Geophys. J. Int. (2004) **158,** 142–168 doi: 10.1111/j.1365-246X.2004.02324.x

Three-dimensional sensitivity kernels for surface wave observables

Ying Zhou, F. A. Dahlen and Guust Nolet

Department of Geosciences, Princeton University, Princeton, NJ 08544, *USA*

Accepted 2004 February 19. Received 2004 February 19; in original form 2003 August 11

SUMMARY

We calculate three dimensional (3-D) sensitivity kernels for fundamental-mode surface wave observables based on the single-scattering (Born) approximation. The sensitivity kernels for measured phases, amplitudes and arrival angles are formulated in the framework of surface wave mode summation. We derive kernels for cross-spectral multitaper measurements; as a special case, the results are applicable to single-taper measurements. Cross-branch mode-coupling effects are fully accounted for in the kernels; however, these effects can probably be ignored at the present level of spatial resolution in global phase-delay tomography. The narrowly concentrated spectra of the windows and tapers commonly used in global surface wave studies enable the kernels to be computed extremely efficiently.

Key words: Fréchet derivatives, global seismology, mode coupling, sensitivity, surface waves.

1 INTRODUCTION

Surface wave tomography based upon great-circle ray theory has been used with great success during the past three decades to constrain the large-scale 3-D heterogeneity of the lithosphere and upper mantle. While the growing abundance of seismic data promotes progress in retrieving better-resolved images with smaller-scale details, ray theory, upon which most surface wave tomography is based, has its theoretical limitations. Ray theory assumes that the frequency of seismic waves is infinite; thereby, it breaks down whenever the length scale of the heterogeneity is comparable to the characteristic wavelength of the seismic waves. Due to their finite frequency, surface waves are sensitive to 3-D structure off of the source–receiver great-circle ray. An approach beyond ray theory aiming at resolving small-scale structures is required to take into account the finite-frequency effects of surface waves. Recent studies have shown a growing appreciation of the finite-frequency properties of seismic body waves (Yomogida 1992; Marquering *et al.* 1998; Friederich 1999; Marquering *et al.* 1999; Dahlen *et al.* 2000; Hung *et al.* 2000; Dalkolmo & Friederich 2000; Zhao *et al.* 2000; Kárason & van der Hilst 2001; Montelli *et al.* 2003); surface waves (Snieder 1986; Snieder & Nolet 1987; Yomogida & Aki 1987; Friederich *et al.* 1993; Meier *et al.* 1997; Capdeville *et al.* 2000; Clévédé 2000; Spetzler *et al.* 2001, 2002; Ritzwoller *et al.* 2002; Yoshizawa & Kennett 2002) and low-frequency normal modes (Woodhouse & Girnius 1982; Dahlen 1987; Romanowicz 1987).

In global surface wave tomography, fundamental-mode surface wave phase delays are widely used to obtain phase-velocity maps at different frequencies, which then can be used to constrain 3-D Earth structure (e.g. Laske & Masters 1996; Ekström *et al.* 1997). The interpretation of surface wave amplitudes can be complicated by effects other than lateral heterogeneities, notably the Earth's 3-D attenuation structure. Nevertheless, amplitudes and, especially, arrival angles have occasionally been used as complementary information to phase-delay measurements (Laske *et al.* 1994; Laske 1995; Laske & Masters 1996; Yoshizawa *et al.* 1999; Larson & Ekström 2002). In this paper we calculate 3-D Fréchet sensitivity kernels for all three types of measurements: phase delays, amplitudes and arrival angles. We derive 3-D surface wave sensitivity kernels based on the single-scattering (Born) approximation, formulated in the framework of surface wave mode summation.

Measurements of surface wave phase delays, amplitudes and arrival angles are often made with tapered/windowed seismograms. We focus our consideration on fundamental-mode surface wave measurements. We derive the 3-D sensitivity kernels for multitaper measurements, and document how the tapering/windowing affects the geometry of the 3-D sensitivity kernels. We also investigate the effects of surface wave mode coupling on the sensitivity kernels. In the last section, we propose an approximation approach, to speed up the computation of sensitivity kernels for large data sets.

2 PRELIMINARIES

We consider an isotropic, elastic earth model occupying a volume $\oplus$. We denote the density by ρ, the Lamé parameters by λ and μ, the associated compressional wave speed by $\alpha = [(\lambda + 2\mu)/\rho]^{1/2}$ and the associated shear wave speed by $\beta = (\mu/\rho)^{1/2}$. We start with a

spherically symmetric reference earth model, in which the parameters ρ, λ, μ, α and β depend only on the radius r. This reference earth model is then subjected to an infinitesimal perturbation in the density and the Lamé parameters:

$$\rho \to \rho + \delta\rho, \quad \lambda \to \lambda + \delta\lambda, \quad \mu \to \mu + \delta\mu. \tag{2.1}$$

The associated perturbations in the compressional wave and shear wave speeds are

$$\beta \to \beta + \delta\beta, \quad \alpha \to \alpha + \delta\alpha, \tag{2.2}$$

where

$$2\rho\alpha\delta\alpha = \delta\lambda + 2\delta\mu - \alpha^2\delta\rho, \quad 2\rho\beta\delta\beta = \delta\mu - \beta^2\delta\rho. \tag{2.3}$$

The model perturbations $\delta\rho$, $\delta\lambda$, $\delta\mu$, $\delta\alpha$ and $\delta\beta$ are 3-D functions of position $\mathbf{x}$ in the background spherical earth $\oplus$. We do not consider perturbations in the locations of discontinuity surfaces in this paper.

In response to the infinitesimal model perturbation, the surface wave observables—phase ϕ, amplitude A and arrival angle ξ—deviate from the predictions based on the spherically symmetric reference earth model:

$$\phi \to \phi + \delta\phi, \quad A \to A + \delta A, \quad \xi \to \xi + \delta\xi. \tag{2.4}$$

For brevity, we shall employ a generic shorthand notation for both the data and model perturbations:

$$\delta d(\omega): \quad \text{shorthand for } \delta\phi, \delta(\ln A), \delta\xi, \tag{2.5}$$

$$\delta m(\mathbf{x}): \quad \text{shorthand for } \delta\rho/\rho, \delta\beta/\beta, \delta\alpha/\alpha. \tag{2.6}$$

We seek a linear relation between data δd and the fractional model perturbation, δm:

$$\delta d(\omega) = \int\int\int_{\oplus} K_d^m(\mathbf{x}, \omega)\delta m(\mathbf{x})\, d^3\mathbf{x}, \tag{2.7}$$

where the volumetric integration is over all points $\mathbf{x}$ in the 3-D earth, and the quantity $K_d^m(\mathbf{x}, \omega)$ is the so-called Fréchet sensitivity kernel. There are a total of three phase sensitivity kernels $K_\phi^{\alpha,\beta,\rho}(\mathbf{x}, \omega)$, three amplitude sensitivity kernels $K_A^{\alpha,\beta,\rho}(\mathbf{x}, \omega)$, and three arrival-angle sensitivity kernels $K_\xi^{\alpha,\beta,\rho}(\mathbf{x}, \omega)$.

In following sections, we shall consider functions of time t as well as functions of angular frequency ω. We use the Fourier sign convention

$$f(\omega) = \int_{-\infty}^{\infty} f(t)\mathrm{e}^{-i\omega t}\, dt, \qquad f(t) = \frac{1}{\pi}\mathrm{Re}\int_0^{\infty} f(\omega)\mathrm{e}^{i\omega t}\, d\omega, \tag{2.8}$$

where the time-domain signal $f(t)$ is presumed to be real.

2.1 Surface wave Green's tensor

In the frequency domain, the far-field Green's tensor $\boldsymbol{G}_{\mathrm{rs}}(\omega)$, representing the displacement response at the receiver $\mathbf{x}_\mathrm{r} = (r_\mathrm{r}, \theta_\mathrm{r}, \phi_\mathrm{r})$ to an impulsive source at the source $\mathbf{x}_\mathrm{s} = (r_\mathrm{s}, \theta_\mathrm{s}, \phi_\mathrm{s})$, can be written as a summation over all surface wave modes (Snieder & Nolet 1987; Dahlen & Tromp 1998, Section 11.3):

$$\boldsymbol{G}_{\mathrm{rs}}(\omega) = \sum_\sigma \frac{\mathbf{p}_\mathrm{s}^*\mathbf{p}_\mathrm{r}\mathrm{e}^{-i(k\Delta - n\pi/2 + \pi/4)}}{(cCI)\sqrt{8\pi k|\sin\Delta|}}, \tag{2.9}$$

where Δ is the angular arc length from the source to the receiver, and the asterisk denotes the complex conjugate. The index $\sigma = 0, 1, 2, \ldots$ specifies the surface wave mode branch, and $k = k_\sigma$ is the the angular wavenumber of the σth surface wave mode. The integer $n = n_\sigma$ is the polar passage index, or the number of times that the wave train passes through the source or its antipode: a minor-arc wave train has no polar passages ($n = 0$), whereas a major-arc wave train has one antipodal passage ($n = 1$). The vector $\mathbf{p} = \mathbf{p}_\sigma$ is the polarization vector of the σth mode (Snieder & Nolet 1987):

$$\mathbf{p} = \hat{\mathbf{r}}U - i\hat{\mathbf{k}}V + i(\hat{\mathbf{r}} \times \hat{\mathbf{k}})W, \tag{2.10}$$

where $U = U_\sigma(r)$, $V = V_\sigma(r)$ and $W = W_\sigma(r)$ are the displacement eigenfunctions of the σth mode surface wave; and $\hat{\mathbf{r}}$, $\hat{\mathbf{k}}$ and $\hat{\mathbf{r}} \times \hat{\mathbf{k}}$ are the vertical, radial and transverse unit vectors (Fig. 1). The roman subscripts s and r in the surface wave polarization vectors $\mathbf{p}_\mathrm{s}$ and $\mathbf{p}_\mathrm{r}$ denote evaluation at the source $\mathbf{x}_\mathrm{s}$ or at the receiver $\mathbf{x}_\mathrm{r}$. The quantity $c = \omega/k$ is the phase velocity c_σ, and $C = d\omega/dk$ is the group velocity C_σ, both measured in rad s^{-1} on the unit sphere. Finally, the quantity $I = I_\sigma$ is a normalization integral, given by

$$I = \int_0^a \rho(r)[U^2(r) + V^2(r) + W^2(r)]r^2\, dr, \tag{2.11}$$

where a is the radius of the Earth. In the rest of the paper we shall use the surface wave normalization in Tromp & Dahlen (1992),

$$cCI = 1\,\mathrm{N\,m}. \tag{2.12}$$

2.2 Born approximation—Green's tensor perturbation

As a result of the earth model perturbation $\lambda \to \lambda + \delta\lambda$, $\rho \to \rho + \delta\rho$, $\mu \to \mu + \delta\mu$, the associated surface wave Green's tensor is perturbed by

$$\boldsymbol{G}_{\rm rs}(\omega) \to \boldsymbol{G}_{\rm rs}(\omega) + \delta\boldsymbol{G}_{\rm rs}(\omega). \tag{2.13}$$

In the single-scattering (Born) approximation, the Green's tensor perturbation $\delta\boldsymbol{G}_{\rm rs}(\omega)$ is given by (Dahlen *et al.* 2000)

$$\begin{aligned}\delta\boldsymbol{G}_{\rm rs}(\omega) = &\int\!\!\int\!\!\int_{\oplus} \delta\rho(\mathbf{x})\big(\omega^2 \boldsymbol{G}_{\rm rx}\cdot\boldsymbol{G}_{\rm xs}\big)\, d^3\mathbf{x}\\ &- \int\!\!\int\!\!\int_{\oplus} \delta\lambda(\mathbf{x})\big(\nabla_{\rm x}\cdot\boldsymbol{G}_{\rm rx}^{\rm T}\big)(\nabla_{\rm x}\cdot\boldsymbol{G}_{\rm xs})\, d^3\mathbf{x}\\ &- \int\!\!\int\!\!\int_{\oplus} \delta\mu(\mathbf{x})(\nabla_{\rm x}\boldsymbol{G}_{\rm rx})^{\rm T} : \big[\nabla_{\rm x}\boldsymbol{G}_{\rm xs} + (\nabla_{\rm x}\boldsymbol{G}_{\rm xs})^{\rm T}\big]\, d^3\mathbf{x},\end{aligned} \tag{2.14}$$

where $\nabla_{\rm x}$ is the spatial gradient with respect to $\mathbf{x}$, and the superscript T denotes the transpose over the first and second indices of either a second-order or third-order tensor. The quantity $\boldsymbol{G}_{\rm xs}(\omega)$ is the unperturbed Green's tensor for an impulsive source at $\mathbf{x}_{\rm s}$ and a receiver at the heterogeneity (scatterer) $\mathbf{x}$, whereas the quantity $\boldsymbol{G}_{\rm rx}(\omega)$ is the Green's tensor for an impulsive source at the scatterer $\mathbf{x}$ and a receiver at $\mathbf{x}_{\rm r}$. The Green's tensor perturbation $\boldsymbol{\delta G}_{\rm rs}(\omega)$ involves volumetric integrations over all of the 3-D heterogeneities (scatterers) $\mathbf{x}$ in $\oplus$.

Upon substituting the Green's tensor, eq. (2.9), into eq. (2.14), and employing the normalization in eq. (2.12), the Green's tensor perturbation $\boldsymbol{\delta G}_{\rm rs}(\omega)$ becomes a double summation over all surface wave modes

$$\boldsymbol{\delta G}_{\rm rs}(\omega) = \sum_{\sigma'}\sum_{\sigma''}\int\!\!\int\!\!\int_{\oplus} \frac{\mathbf{p}_{\rm s}'^{*}\mathbf{p}_{\rm r}''\,{\rm e}^{-i[k'\Delta' + k''\Delta'' - (n'+n''-1)\pi/2]}}{\sqrt{8\pi k'|\sin\Delta'|}\sqrt{8\pi k''|\sin\Delta''|}}\,{}_{\sigma'}\Omega_{\sigma''}\, d^3\mathbf{x}, \tag{2.15}$$

where we have used a single prime to denote the source-to-scatterer leg and a double prime to denote the scatterer-to-receiver leg of the scattered wave (Fig. 1). The indices σ' and σ'' stand for the surface wave mode along the source-to-scatterer and scatterer-to-receiver legs, of arclength Δ' and Δ'' respectively. The vector $\mathbf{p}_{\rm s}'$ is shorthand for $\mathbf{p}_{{\rm s}\sigma'}$, the polarization vector of the σ'th surface wave mode at the source $\mathbf{x}_{\rm s}$, whereas $\mathbf{p}_{\rm r}''$ is shorthand for $\mathbf{p}_{{\rm r}\sigma''}$, the polarization vector of the σ''th surface wave mode at the receiver $\mathbf{x}_{\rm r}$. Likewise, we abbreviate $k' = k_{\sigma'}$, $k'' = k_{\sigma''}$ and $n' = n_{\sigma'}$, $n'' = n_{\sigma''}$. The total phase delay of the scattered surface wave is represented by the phase term ${\rm e}^{-i[k'\Delta' + k''\Delta'' + (n'+n''-1)\pi/2]}$; the geometrical spreading along path′ and path″ is accounted for by the factors $(8\pi k'|\sin\Delta'|)^{-1/2}$ and $(8\pi k''|\sin\Delta''|)^{-1/2}$, respectively. The strength of the single scattering is represented by the 3-D interaction coefficient ${}_{\sigma'}\Omega_{\sigma''}$, which is a linear function of the model perturbations $\delta\lambda$, $\delta\mu$ and $\delta\rho$:

$${}_{\sigma'}\Omega_{\sigma''} = \delta\rho\omega^2(\mathbf{p}'\cdot\mathbf{p}''^{*}) - \delta\lambda({\rm tr}\boldsymbol{E}')({\rm tr}\boldsymbol{E}''^{*}) - 2\delta\mu(\boldsymbol{E}' : \boldsymbol{E}''^{*}), \tag{2.16}$$

where

$$\boldsymbol{E} = \frac{1}{2}[\nabla\mathbf{p} + (\nabla\mathbf{p})^{\rm T}] \tag{2.17}$$

is the surface wave strain tensor. The quantities $\boldsymbol{E}' = \boldsymbol{E}_{\sigma'}(\mathbf{x},\omega)$ and $\boldsymbol{E}'' = \boldsymbol{E}_{\sigma''}(\mathbf{x},\omega)$ are the strain tensors of surface wave modes σ' and σ'' evaluated at the scatterer $\mathbf{x}$. We show in the Appendix that the interaction coefficient ${}_{\sigma'}\Omega_{\sigma''}(\mathbf{x},\omega)$ is a linear function of the fractional model perturbations $\delta\rho/\rho$, $\delta\beta/\beta$ and $\delta\alpha/\alpha$:

$${}_{\sigma'}\Omega_{\sigma''} = {}_{\sigma'}\Omega^{m}_{\sigma''}\delta m = {}_{\sigma'}\Omega^{\alpha}_{\sigma''}\left(\frac{\delta\alpha}{\alpha}\right) + {}_{\sigma'}\Omega^{\beta}_{\sigma''}\left(\frac{\delta\beta}{\beta}\right) + {}_{\sigma'}\Omega^{\rho}_{\sigma''}\left(\frac{\delta\rho}{\rho}\right). \tag{2.18}$$

The detailed dependence of the scattering coefficients ${}_{\sigma'}\Omega^{\rho}_{\sigma''}$, ${}_{\sigma'}\Omega^{\beta}_{\sigma''}$, ${}_{\sigma'}\Omega^{\alpha}_{\sigma''}$ upon the scattering angle η (Fig. 1) is given in the Appendix.

2.3 Moment tensor response

The surface wave displacement response $s(\omega)$ to a source with frequency-dependent moment tensor $\boldsymbol{M} = \boldsymbol{M}(\omega)$ is (Snieder & Nolet 1987; Dahlen & Tromp 1998, Section 11.4)

$$s(\omega) = (i\omega)^{-1}\big[\boldsymbol{M} : \nabla_{\rm s}\boldsymbol{G}_{\rm rs}^{\rm T}(\omega)\big]\cdot\hat{\boldsymbol{\nu}}, \tag{2.19}$$

where $\hat{\boldsymbol{\nu}}$ is the unit vector describing the polarization of the seismometer at the receiver. To lowest order, the gradient $\nabla_{\rm s}$ acts only upon the oscillatory term ${\rm e}^{-ik\Delta}$ in eq. (2.9) and upon the surface wave polarization vector at the source $\mathbf{p}_{\rm s}$, yielding

$$s(\omega) = \sum_{\sigma} \underbrace{(i\omega)^{-1}\big(\boldsymbol{M} : \boldsymbol{E}_{\rm s}^{*}\big)}_{\substack{\text{source}\\ \text{radiation}}} \times \underbrace{\left(\frac{{\rm e}^{-i(k\Delta - n\pi/2 + \pi/4)}}{\sqrt{8\pi k|\sin\Delta|}}\right)}_{\text{geometrical ray path}} \times \underbrace{\mathbf{p}_{\rm r}\cdot\hat{\boldsymbol{\nu}}}_{\substack{\text{receiver}\\ \text{polarization}}}. \tag{2.20}$$

It is convenient in what follows to introduce a revised notation for the source and receiver terms in the above equation. The source radiation term will be written as

$$\mathcal{S} = \mathcal{S}_{\sigma}(\zeta) = (i\omega)^{-1}\big(\boldsymbol{M} : \boldsymbol{E}_{\rm s}^{*}\big), \tag{2.21}$$

where ζ is the source take-off angle measured counter-clockwise from the south (Fig. 1), and $\boldsymbol{E}_{\rm s}$ is the surface wave strain tensor at the source $\mathbf{x}_{\rm s}$. In detail (Dahlen & Tromp 1998, Section 11.4),

$$\begin{aligned}\mathcal{S} = &-i\omega^{-1}\big[M_{rr}\dot{U}_{\rm s} + (M_{\theta\theta}+M_{\phi\phi})r_{\rm s}^{-1}\big(U_{\rm s} - \tfrac{1}{2}kV_{\rm s}\big)\big]\\ &+\omega^{-1}(-1)^n\big(\dot{V}_{\rm s} - r_{\rm s}^{-1}V_{\rm s} + kr_{\rm s}^{-1}U_{\rm s}\big)(M_{r\phi}\sin\zeta + M_{r\theta}\cos\zeta)\\ &+i\omega^{-1}kr_{\rm s}V_{\rm s}\big[M_{\theta\phi}\sin 2\zeta + \tfrac{1}{2}(M_{\theta\theta}-M_{\phi\phi}\cos 2\zeta)\big]\\ &+\omega^{-1}(-1)^n(\dot{W}_{\rm s} - r_{\rm s}^{-1}W_{\rm s})(M_{r\theta}\sin\zeta - M_{r\phi}\cos\zeta)\\ &+i\omega^{-1}kr_{\rm s}^{-1}W_{\rm s}\big[\tfrac{1}{2}(M_{\theta\theta}-M_{\phi\phi})\sin 2\zeta - M_{\theta\phi}\cos 2\zeta\big].\end{aligned} \tag{2.22}$$

The quantities $U_{\rm s}, V_{\rm s}, W_{\rm s}$ and $\dot{U}_{\rm s}$, $\dot{V}_{\rm s}$ and $\dot{W}_{\rm s}$ are shorthand for $U_\sigma(r_{\rm s}), V_\sigma(r_{\rm s}), W_\sigma(r_{\rm s})$ and $\dot{U}_\sigma(r_{\rm s})$, $\dot{V}_\sigma(r_{\rm s})$ $\dot{W}_\sigma(r_{\rm s})$, the surface wave displacement eigenfunctions and their radial derivatives evaluated at the radius of the seismic source, $r = r_{\rm s}$. The quantities M_{rr}, $M_{\phi\phi}$, $M_{\theta\theta}$, $M_{r\theta}$, $M_{r\phi}$ and $M_{\theta\phi}$ are the six independent elements of the moment tensor $\boldsymbol{M}(\omega)$. The receiver polarization term will be denoted by

$$\mathcal{R} = \mathbf{p}_{\rm r}\cdot\hat{\boldsymbol{\nu}} = [\hat{\mathbf{r}}_{\rm r}U_{\rm r} - i\hat{\mathbf{k}}_{\rm r}V_{\rm r} + i(\hat{\mathbf{r}}_{\rm r}\times\hat{\mathbf{k}}_{\rm r})W_{\rm r}]\cdot\hat{\boldsymbol{\nu}}, \tag{2.23}$$

where $U_{\rm r}, V_{\rm r}$ and $W_{\rm r}$ are shorthand for $U_\sigma(r_{\rm r}), V_\sigma(r_{\rm r})$ and $W_\sigma(r_{\rm r})$, the displacement eigenfunction of surface wave mode σ evaluated at the radius of the receiver, $r = r_{\rm r}$. For vertical, radial and transverse component seismic recordings,

$$\hat{\boldsymbol{\nu}} = \begin{cases}\hat{\mathbf{r}}_{\rm r} & \text{vertical component,}\\ \hat{\mathbf{k}}_{\rm r} & \text{radial component,}\\ \hat{\mathbf{r}}_{\rm r}\times\hat{\mathbf{k}}_{\rm r} & \text{transverse component;}\end{cases} \tag{2.24}$$

and the associated receiver term $\mathcal{R} = \mathcal{R}_\sigma$ is given by

$$\mathcal{R} = \begin{cases}U_{\rm r} & \text{vertical component,}\\ -iV_{\rm r} & \text{radial component,}\\ iW_{\rm r} & \text{transverse component.}\end{cases} \tag{2.25}$$

The summation over all possible surface wave modes in eq. (2.20) provides a complete seismogram with all seismic phases. In this paper, we focus upon the measurements of fundamental-mode surface waves. We shall therefore henceforth drop the mode summation notation, and write the displacement in the unperturbed earth model as

$$s(\omega) = \underbrace{\mathcal{S}}_{\substack{\text{source}\\ \text{radiation}}} \times \underbrace{\left(\frac{\mathrm{e}^{-i(k\Delta - n\pi/2+\pi/4)}}{\sqrt{8\pi k|\sin\Delta|}}\right)}_{\text{geometrical ray path}} \times \underbrace{\mathcal{R}}_{\substack{\text{receiver}\\ \text{polarization}}}. \tag{2.26}$$

The three component seismograms—vertical component $u(\omega)$, radial component $v(\omega)$ and transverse component $w(\omega)$—are

$$\begin{pmatrix}u(\omega)\\ v(\omega)\\ w(\omega)\end{pmatrix} = \mathcal{S}\times\left(\frac{\mathrm{e}^{-i(k\Delta - n\pi/2+\pi/4)}}{\sqrt{8\pi k|\sin\Delta|}}\right)\times\begin{pmatrix}U_{\rm r}\\ -iV_{\rm r}\\ iW_{\rm r}\end{pmatrix}. \tag{2.27}$$

The surface wave mode in eqs (2.26) and (2.27) is either the fundamental-mode Love wave or the fundamental-mode Rayleigh wave, depending on the measurement of interest.

2.4 Perturbed moment tensor response

In the presence of 3-D heterogeneities $\delta m(\mathbf{x})$, the displacement field can be decomposed into two contributing components: the displacement field in the unperturbed earth model $s(\omega)$, and the scattered wavefield $\delta s(\omega)$ due to the model perturbations:

$$s(\omega) \to s(\omega) + \delta s(\omega). \tag{2.28}$$

The scattered wave $\delta s(\omega)$ generated by a moment tensor source $\boldsymbol{M}(\omega)$ can be obtained from the Green's tensor perturbation via the analogue of eq. (2.19):

$$\delta s(\omega) = (i\omega)^{-1}\boldsymbol{M} : \nabla_{\rm s}\big[\delta\boldsymbol{G}_{\rm rs}^{\rm T}(\omega)\big]\cdot\hat{\boldsymbol{\nu}}. \tag{2.29}$$

Upon substituting the expression for $\delta\boldsymbol{G}_{\rm rs}$ from eq. (2.15), and making the same approximation to the operator $\nabla_{\rm s}$ as in eq. (2.20), we obtain

$$\begin{aligned}\delta s(\omega) = \sum_{\sigma'}\sum_{\sigma''}\int\!\!\int\!\!\int_{\oplus} &\underbrace{\mathcal{S}'}_{\substack{\text{source}\\ \text{radiation}}} \times \underbrace{\left(\frac{\mathrm{e}^{-i(k'\Delta' - n'\pi/2+\pi/4)}}{\sqrt{8\pi k'|\sin\Delta'|}}\right)}_{\text{mode }\sigma'\text{ along path}'} \times \underbrace{{}_{\sigma'}\Omega_{\sigma''}}_{\substack{\text{scattering}\\ \text{interaction}}}\\ &\times \underbrace{\left(\frac{\mathrm{e}^{-i(k''\Delta'' - n''\pi/2+\pi/4)}}{\sqrt{8\pi k''|\sin\Delta''|}}\right)}_{\text{mode }\sigma''\text{ along path}''} \times \underbrace{\mathcal{R}''}_{\substack{\text{receiver}\\ \text{polarization}}}\, d^3\mathbf{x}.\end{aligned} \tag{2.30}$$

Adopting the colourful language of Snieder (1986), we note that every term in the double sum eq. (2.30) can be read from left to right as a 'life history' of a singly scattered wave: the σ'th surface wave mode is excited by the seismic source, with $\mathcal{S}' = \mathcal{S}_{\sigma'}(\zeta')$ accounting for the radiation; the outgoing wave takes the source-to-scatterer path, leading to a phase delay and geometrical spreading as specified in the path$'$ term; the σ'th mode then interacts with the scatterer via the term ${}_{\sigma'}\Omega_{\sigma''}$, leaving as a σ''th surface wave mode, which propagates along the scatterer-to-receiver path, accumulating an additional phase delay and geometrical spreading as specified in the path$''$ term; finally, the displacement of the scattered wave is recorded by the seismometer, with $\mathcal{R}''$ accounting for the receiver polarization (Fig. 1).
For vertical, radial and transverse seismograms, the receiver term is

$$\mathcal{R}'' = \begin{cases} U''_{\rm r} & \text{vertical component,} \\ -i\,V''_{\rm r}\cos(\xi''-\xi) - i\,W''_{\rm r}\sin(\xi''-\xi) & \text{radial component,} \\ i\,W''_{\rm r}\cos(\xi''-\xi) - i\,V''_{\rm r}\sin(\xi''-\xi) & \text{transverse component,} \end{cases} \tag{2.31}$$

where $U''_{\rm r} = U_{\sigma''}(r_{\rm r})$, $V''_{\rm r} = V_{\sigma''}(r_{\rm r})$, $W''_{\rm r} = W_{\sigma''}(r_{\rm r})$, and ξ'' and ξ are the receiver arrival angles of the perturbed σ''th surface wave mode and the unperturbed σth mode, respectively, both measured counter-clockwise from geographical south (Fig. 1). We remind readers that the radial and transverse components are defined with respect to the unperturbed ray, i.e, $\hat{\boldsymbol{\nu}} = \hat{\mathbf{k}}_{\rm r}$ if the recording is on the radial component, and $\hat{\boldsymbol{\nu}} = \hat{\mathbf{r}}_{\rm r} \times \hat{\mathbf{k}}_{\rm r}$ if the recording is on the transverse component.

Upon substituting the compact expression ${}_{\sigma'}\Omega_{\sigma''} = {}_{\sigma'}\Omega^m_{\sigma''}\delta m$ for the interaction coefficient, into eq. (2.30), the displacement of the scattered wave $\delta s(\omega)$ can be expressed as a volumetric integration over all 3-D scatterers $\delta m(\mathbf{x})$:

$$\delta s(\omega) = \int\!\!\int\!\!\int_{\oplus} \mathcal{K}^m(\mathbf{x},\omega)\delta m(\mathbf{x})\, d^3\mathbf{x}, \tag{2.32}$$

where $\mathcal{K}^m(\mathbf{x},\omega)$ is the complex integration kernel for the scattered waveform,

$$\mathcal{K}^m(\mathbf{x},\omega) = \sum_{\sigma'}\sum_{\sigma''} \mathcal{S}' \left(\frac{\mathrm{e}^{-i(k'\Delta' - n'\pi/2 + \pi/4)}}{\sqrt{8\pi k'|\sin\Delta'|}} \right) {}_{\sigma'}\Omega^m_{\sigma''} \left(\frac{\mathrm{e}^{-i(k''\Delta'' - n''\pi/2 + \pi/4)}}{\sqrt{8\pi k''|\sin\Delta''|}} \right) \mathcal{R}''. \tag{2.33}$$

Upon substituting the receiver terms in eq. (2.31) into eqs (2.32)–(2.33), the vertical, radial and transverse component displacements of the scattered wave, $\delta u(\omega)$, $\delta v(\omega)$ and $\delta w(\omega)$ can be likewise expressed as volumetric integrations over all 3-D heterogeneities:

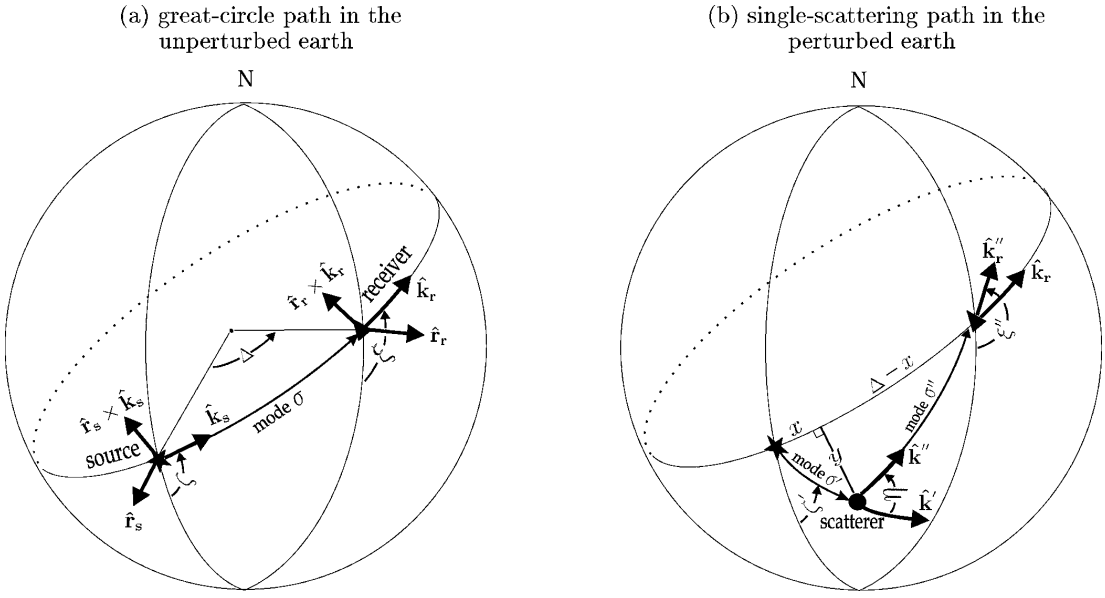

Figure 1. (a) Source–receiver great-circle path in the unperturbed earth. The vectors $\hat{\mathbf{r}}$, $\hat{\mathbf{k}}$ and $\hat{\mathbf{r}} \times \hat{\mathbf{k}}$ are the vertical, radial and transverse unit vectors; roman subscripts s and r denote evaluation at the source or the receiver; σ is the surface wave mode index of the reference ray; Δ is the source–receiver epicentral distance; ζ is the source take-off angle of the reference ray, measured counter-clockwise from geographical south to $\hat{\mathbf{k}}_{\rm s}$; and ξ is the receiver arrival angle of the reference ray, measured counter-clockwise from geographical south to $\hat{\mathbf{k}}_{\rm r}$. (b) Single-scattering path in the perturbed earth; σ' is the mode index of the outgoing wave along the source-to-scatterer path, σ'' is the mode index of the scattered wave along the scatterer-to-receiver path; $\hat{\mathbf{k}}'$ and $\hat{\mathbf{k}}''$ are the unit wavenumber vectors of modes σ' and σ'', evaluated at the scatterer; $\hat{\mathbf{k}}''_{\rm r}$ is the unit wavenumber vector of the scattered surface wave mode σ'' at the receiver; ζ' is the source take-off angle of the outgoing surface wave mode σ'; ξ'' is the receiver arrival angle of the scattered surface wave mode σ''; η is the scattering angle, measured counter-clockwise from $\hat{\mathbf{k}}'$ to $\hat{\mathbf{k}}''$; y is the perpendicular angular distance from the scatterer to the great-circle ray; x and $\Delta - x$ are the distances from the source and receiver to this perpendicular point.

$$\begin{pmatrix}\delta u(\omega)\\ \delta v(\omega)\\ \delta w(\omega)\end{pmatrix} = \int\int\int_{\oplus} \begin{pmatrix}\mathcal{U}^m(\mathbf{x},\omega)\\ \mathcal{V}^m(\mathbf{x},\omega)\\ \mathcal{W}^m(\mathbf{x},\omega)\end{pmatrix} \delta m(\mathbf{x})\, d^3\mathbf{x}. \tag{2.34}$$

The three-component waveform kernels of the scattered waves, $\mathcal{U}^m(\mathbf{x},\omega)$, $\mathcal{V}^m(\mathbf{x},\omega)$, and $\mathcal{W}^m(\mathbf{x},\omega)$ are given explicitly by

$$\begin{aligned}\begin{pmatrix}\mathcal{U}^m(\mathbf{x},\omega)\\ \mathcal{V}^m(\mathbf{x},\omega)\\ \mathcal{W}^m(\mathbf{x},\omega)\end{pmatrix} = \sum_{\sigma'}\sum_{\sigma''} \mathcal{S}' \times \left(\frac{\mathrm{e}^{-i(k'\Delta'-n'\pi/2+\pi/4)}}{\sqrt{8\pi k'|\sin\Delta'|}}\right) \times {}_{\sigma'}\Omega^m_{\sigma''} \\ \times \left(\frac{\mathrm{e}^{-i(k''\Delta''-n''\pi/2+\pi/4)}}{\sqrt{8\pi k''|\sin\Delta''|}}\right) \times \begin{pmatrix} U''_{\mathrm{r}} \\ -i\,V''_{\mathrm{r}}\cos(\xi''-\xi) - i\,W''_{\mathrm{r}}\sin(\xi''-\xi) \\ i\,W''_{\mathrm{r}}\cos(\xi''-\xi) - i\,V''_{\mathrm{r}}\sin(\xi''-\xi)\end{pmatrix}.\end{aligned} \tag{2.35}$$

All of the above results are either explicit or implicit in Snieder & Nolet (1987) and other later references; we have reviewed them in some detail here simply to establish a notation for the considerations that follows.

3 SINGLE-FREQUENCY SENSITIVITY KERNELS

We begin by considering monochromatic frequency measurements made using unwindowed recordings in the time domain. Phase and amplitude measurements made on a single component are treated in Section 3.1, and arrival-angle measurements made using the two horizontal components are treated in Section 3.2.

3.1 Phase and amplitude kernels

Let $o(\omega)$ be the observed waveform recorded on either the $\hat{\mathbf{r}}_{\mathrm{r}}$ (vertical), $\hat{\mathbf{k}}_{\mathrm{r}}$ (radial) or $\hat{\mathbf{r}}_{\mathrm{r}} \times \hat{\mathbf{k}}_{\mathrm{r}}$ (transverse) component, and let $s(\omega)$ in eq. (2.26) be the associated waveform in the unperturbed earth. We seek a transfer function $T(\omega)$ that satisfies

$$[o(\omega) - T(\omega)s(\omega)]^2 = \text{minimum}. \tag{3.1}$$

In this single-observation case, the transfer function is simply the spectral division,

$$T(\omega) = \frac{o(\omega)}{s(\omega)}. \tag{3.2}$$

In the idealized unperturbed earth, where the observed and synthetic waveforms coincide, the transfer function (in the absence of noise) is simply unity, $T(\omega) = 1$. In the perturbed earth, the observed seismogram is contaminated by singly scattered waves. We write the spherically symmetric synthetic in the form $s(\omega) = A\mathrm{e}^{-i\phi}$, and the perturbed observation as $o(\omega) = (A + \delta A)\mathrm{e}^{-i(\phi+\delta\phi)}$. In the Born approximation, the observation $o(\omega)$ is given by

$$o(\omega) = s(\omega) + \delta s(\omega), \tag{3.3}$$

where $\delta s(\omega)$ is the displacement spectrum of the scattered wave, given by eq. (2.30). The transfer function is perturbed away from unity:

$$T(\omega) = 1 + \delta T(\omega), \tag{3.4}$$

where

$$\delta T(\omega) = \frac{\delta s(\omega)}{s(\omega)}. \tag{3.5}$$

Correct to first order in the small perturbations,

$$\delta T(\omega) \approx \ln T(\omega) = \delta \ln A(\omega) - i\delta\phi(\omega), \tag{3.6}$$

where

$$\delta\phi(\omega) = -\mathrm{Im}\left(\frac{\delta s}{s}\right), \qquad \delta \ln A(\omega) = \mathrm{Re}\left(\frac{\delta s}{s}\right). \tag{3.7}$$

Upon substituting eqs (2.26) and (2.30) for $s(\omega)$ and $\delta s(\omega)$ into eqs (3.7), we find that the phase and amplitude variations $\delta\phi(\omega)$ and $\delta\ln A(\omega)$ in the perturbed earth model are linearly related to the 3-D heterogeneities $\delta m(\mathbf{x})$ by

$$\delta\phi(\omega) = \int\int\int_{\oplus} K^m_\phi(\mathbf{x},\omega)\delta m(\mathbf{x})\, d^3\mathbf{x}, \quad \delta \ln A(\omega) = \int\int\int_{\oplus} K^m_A(\mathbf{x},\omega)\delta m(\mathbf{x})\, d^3\mathbf{x}, \tag{3.8}$$

where the phase and amplitude sensitivity kernels $K^m_\phi(\mathbf{x},\omega)$ and $K^m_A(\mathbf{x},\omega)$ are

$$K^m_\phi(\mathbf{x},\omega) = -\mathrm{Im}\left(\sum_{\sigma'}\sum_{\sigma''} \frac{\mathcal{S}'_{\sigma'}\Omega^m_{\sigma''}\mathcal{R}''\mathrm{e}^{-i[k'\Delta'+k''\Delta''-k\Delta-(n'+n''-n)\pi/2+\pi/4]}}{\mathcal{S}\mathcal{R}\sqrt{8\pi(k'k''/k)(|\sin\Delta'||\sin\Delta''|/|\sin\Delta|)}}\right), \tag{3.9}$$

$$K_A^m(\mathbf{x},\omega) = \mathrm{Re}\left(\sum_{\sigma'}\sum_{\sigma''}\frac{\mathcal{S}'_{\sigma'}\Omega^m_{\sigma''}\mathcal{R}''\mathrm{e}^{-i[k'\Delta'+k''\Delta''-k\Delta-(n'+n''-n)\pi/2+\pi/4]}}{\mathcal{S}\mathcal{R}\sqrt{8\pi(k'k''/k)(|\sin\Delta'||\sin\Delta''|/|\sin\Delta|)}}\right). \tag{3.10}$$

3.2 Arrival-angle kernels

We consider only measurements of the surface wave polarization in the horizontal plane. The perturbation in arrival angle $\delta\xi(\omega)$ is defined as the angle between the major axis of the polarization of the surface wave in the perturbed earth and the polarization vector of the unperturbed ray, both evaluated at the receiver. We seek sensitivity kernels for arrival-angle measurements, $K^m_\xi(\mathbf{x},\omega)$, which satisfy

$$\delta\xi(\omega) = \int\int\int_\oplus K^m_\xi(\mathbf{x},\omega)\delta m(\mathbf{x})\,d^3\mathbf{x}. \tag{3.11}$$

Let $\mathbf{o}(\omega)$ be the observed horizontal waveform, and following Park *et al.* (1987) and Laske & Masters (1996), define the normalized 2×2 spectral density matrix

$$\mathbf{S}(\omega) = \frac{\mathbf{o}(\omega)\mathbf{o}^*(\omega)}{||\mathbf{o}(\omega)||^2}. \tag{3.12}$$

The matrix in eq. (3.12) is Hermitian, $\mathbf{S}^{\mathrm{H}}(\omega) = \mathbf{S}(\omega)$, so it can be diagonalized,

$$\mathbf{S} = \lambda_1\hat{\mathbf{e}}_1\hat{\mathbf{e}}_1^* + \lambda_2\hat{\mathbf{e}}_2\hat{\mathbf{e}}_2^*, \quad \text{where} \quad \hat{\mathbf{e}}_i\cdot\hat{\mathbf{e}}_j^* = \delta_{ij}. \tag{3.13}$$

In the case of a single frequency measurement, the two eigenvalues are $\lambda_1 = 1$ and $\lambda_2 = 0$; and the major eigenvector is $\hat{\mathbf{e}}_1 = \mathbf{o}(\omega)/||\mathbf{o}(\omega)||$. The horizontal particle motion at an angular frequency ω is an ellipse defined by

$$\mathbf{o}(t) = \mathrm{Re}\big(\hat{\mathbf{e}}_1\mathrm{e}^{i\omega t}\big). \tag{3.14}$$

The major axis of this ellipse can be determined at the time $t = t_{\mathrm{m}}$, when the horizontal surface wave displacement is greatest (Fig. 2)

$$\big|\mathrm{Re}\big(\hat{\mathbf{e}}_1\mathrm{e}^{i\omega t_{\mathrm{m}}}\big)\big| = \text{maximum}. \tag{3.15}$$

The perturbed polarization vector aligned with this major axis is rotated counter-clockwise from the polarization vector of the corresponding unperturbed wave in a spherically symmetric earth by an amount (Park *et al.* 1987)

$$\delta\xi(\omega) = \begin{cases} -\mathrm{Re}\left[\arctan\left(\dfrac{\hat{\mathbf{k}}_{\mathrm{r}}\cdot\hat{\mathbf{e}}_1}{(\hat{\mathbf{r}}_{\mathrm{r}}\times\hat{\mathbf{k}}_{\mathrm{r}})\cdot\hat{\mathbf{e}}_1}\right)\right] & \text{for Love waves,} \\ \mathrm{Re}\left[\arctan\left(\dfrac{(\hat{\mathbf{r}}_{\mathrm{r}}\times\hat{\mathbf{k}}_{\mathrm{r}})\cdot\hat{\mathbf{e}}_1}{\hat{\mathbf{k}}_{\mathrm{r}}\cdot\hat{\mathbf{e}}_1}\right)\right] & \text{for Rayleigh waves.} \end{cases} \tag{3.16}$$

In the Born approximation, the observed horizontal waveform is given by

$$\mathbf{o}(\omega) = (v+\delta v)\hat{\mathbf{k}}_{\mathrm{r}} + (w+\delta w)(\hat{\mathbf{r}}_{\mathrm{r}}\times\hat{\mathbf{k}}_{\mathrm{r}}). \tag{3.17}$$

Correct to first order, the normalized spectral density matrix is

$$\mathbf{S} = \begin{cases} \begin{pmatrix} 0 & \delta v/w \\ \delta v^*/w^* & 1 \end{pmatrix} & \text{for Love waves,} \\ \begin{pmatrix} 1 & \delta w^*/v^* \\ \delta w/v & 0 \end{pmatrix} & \text{for Rayleigh waves.} \end{cases} \tag{3.18}$$

The arrival-angle perturbations for Love and Rayleigh waves are

$$\delta\xi = \begin{cases} -\mathrm{Re}\,(\delta v/w) & \text{for Love waves,} \\ \mathrm{Re}\,(\delta w/v) & \text{for Rayleigh waves.} \end{cases} \tag{3.19}$$

Noting that the horizontal displacements of the scattered waves $\delta v(\omega)$ and $\delta w(\omega)$ are volumetric integrations over 3-D heterogeneities in the perturbed earth, as shown in eq. (2.34), we can write the arrival-angle perturbations $\delta\xi(\omega)$ in the form of eq. (3.11). The associated sensitivity kernel $K^m_\xi(\mathbf{x},\omega)$ for an arrival-angle measurement is

$$K^m_\xi(\mathbf{x},\omega) = \mathrm{Re}\left(\sum_{\sigma'}\sum_{\sigma''}\frac{\mathcal{S}'_{\sigma'}\Omega^m_{\sigma''}\mathcal{F}''\mathrm{e}^{-i[k'\Delta'+k''\Delta''-k\Delta-(n'+n''-n)\pi/2+\pi/4]}}{\mathcal{S}\sqrt{8\pi(k'k''/k)(|\sin\Delta'||\sin\Delta''|/|\sin\Delta|)}}\right) \tag{3.20}$$

where $\mathcal{F}''$ is shorthand for the ratio between the receiver terms $\mathcal{R}''$ and $\mathcal{R}$:

$$\mathcal{F}'' = \begin{cases} [W''\sin(\xi''-\xi) + V''\cos(\xi''-\xi)]/W & \text{for Love waves,} \\ [V''\sin(\xi''-\xi) - W''\cos(\xi''-\xi)]/V & \text{for Rayleigh waves.} \end{cases} \tag{3.21}$$

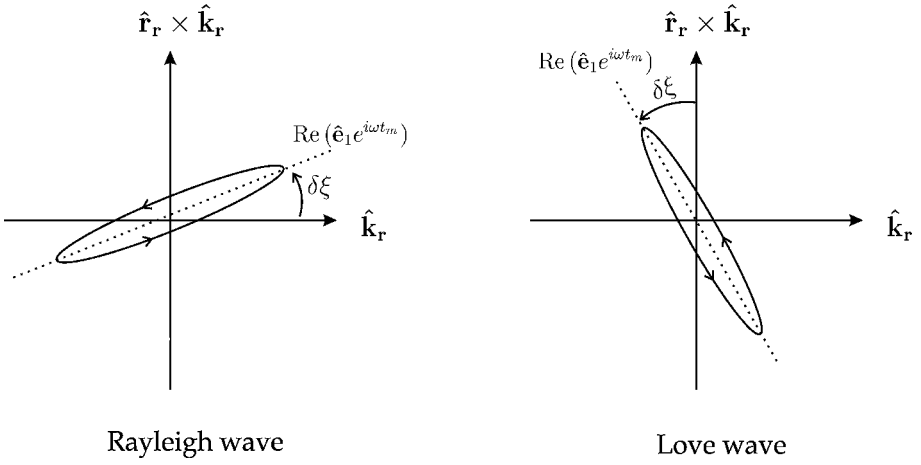

Figure 2. Particle motions of a Rayleigh wave (left) and a Love wave (right) in a perturbed earth. The vector $\mathrm{Re}(\hat{\mathbf{e}}_1 e^{i\omega t_m})$ represents the major axis of the particle motion ellipse. The quantity $\delta\xi$ is the arrival-angle perturbation of the Rayleigh or Love wave, measured in a counter-clockwise direction with respect to the unperturbed arrival direction $\hat{\mathbf{k}}_\mathbf{r}$.

4 SENSITIVITY KERNELS FOR MULTITAPER MEASUREMENTS

The sensitivity kernels $K_d^m(\mathbf{x}, \omega)$ in eqs (3.9), (3.10) and (3.20) are formulated for single-frequency observables $\delta\phi(\omega)$, $\delta \ln A\,(\omega)$ and $\delta\xi(\omega)$. In practice, the spectra $o(\omega)$ and $s(\omega)$ are estimated from a portion of an observed seismogram $o(t)$ in a certain time window. The process of time-domain windowing averages the frequency content of the displacement spectra $o(\omega)$ and $s(\omega)$, and reduces the off-ray sidebands of the kernels. In this section, we derive sensitivity kernel $K_d^m(\mathbf{x}, \omega)$ for measurements made using a cross-spectral multitaper method. As a special case, the results obviously apply to single-taper or even windowed (boxcar taper) measurements.

A multitaper technique (Thomson 1982) using prolate spheroidal eigentapers (Slepian 1978) has been suggested to be an effective means of reducing bias in surface wave spectral estimates (Laske & Masters 1996). The major advantages of the multitaper technique are that the eigentapers have narrowly concentrated spectra, and the eigentapers are orthogonal to each other. As a result, measurements made using multitapers are independent. A reliable spectral estimate can be obtained by forming a least-squares combination of independent measurements; furthermore, these independent measurements provide good estimates of the measurement error. As an example, the first five 2.5π prolate spheroidal eigentapers are plotted in Fig. 3. These 2.5π tapers have their spectral energy mostly confined in the frequency band $(-2.5f, 2.5f)$, where $f = 1/L$ is the Rayleigh frequency, or the reciprocal of the length L of the taper ($L = 800$ s in Fig. 3). Two single tapers, a boxcar taper and a commonly used Hann or cosine taper are also plotted in Fig. 3.

4.1 Multitaper phase and amplitude kernels

We denote the jth taper in the time domain by $h_j(t)$, and its spectrum by $h_j(\omega)$. Let $o_j(\omega)$ be the spectrum of the displacement in the perturbed earth measured with the time-domain taper $h_j(t)$; and let $s_j(\omega)$ be the spectrum of the displacement in the unperturbed earth measured with taper $h_j(t)$. Since windowing in the time domain is equivalent to convolution in the frequency domain, we have

$$o_j(\omega) = o(\omega) \otimes h_j(\omega), \quad s_j(\omega) = s(\omega) \otimes h_j(\omega), \quad \delta s_j(\omega) = \delta s(\omega) \otimes h_j(\omega), \tag{4.1}$$

where $\otimes$ is the convolution operator. Generalizing the transfer function defined in eq. (3.1), the complex transfer function $T(\omega)$ is now required to satisfy (Laske & Masters 1996)

$$\sum_j [o_j(\omega) - T(\omega) s_j(\omega)]^2 = \text{minimum}, \tag{4.2}$$

where the sum is over all the tapers. The phase and amplitude of the transfer function $T(\omega)$ provide estimates of the phase and amplitude variations in the perturbed earth. It can be shown that the transfer function $T(\omega)$ in eq. (4.2) is

$$T(\omega) = \frac{\sum_j o_j s_j^*}{\sum_j s_j s_j^*} = 1 + \delta T(\omega), \tag{4.3}$$

where

$$\delta T(\omega) = \frac{\sum_j \delta s_j s_j^*}{\sum_j s_j s_j^*}. \tag{4.4}$$

Correct to first order in the small perturbations,

$$\delta T(\omega) \approx \ln T(\omega) = \delta \ln A(\omega) - i\delta\phi(\omega), \tag{4.5}$$

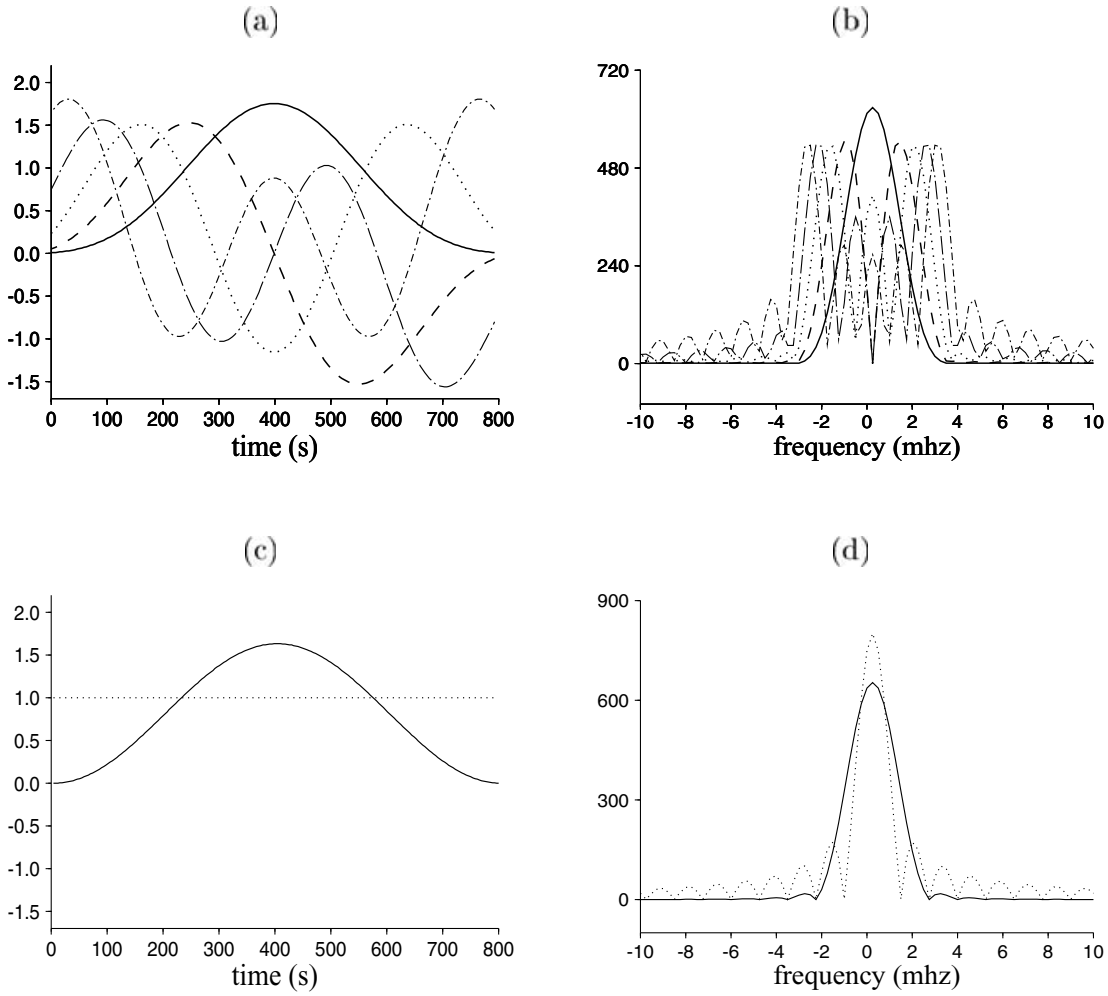

Figure 3. (a) The first five 2.5π prolate spheroidal eigentapers, for an 800 s record; the line styles in the order of the eigentapers are solid, dashed, dotted, long dash-dot and short dash-dot. (b) Spectral amplitudes of the five 2.5π multitapers; the spectra of the 2.5π tapers are narrowly concentrated in the frequency band $(-2.5/L, 2.5/L)$, where L is the length of the taper in seconds. (c) An 800 s cosine taper (solid line) and a boxcar taper (dotted line) of the same length. (d) Spectral amplitudes of the cosine taper (solid line) and the boxcar taper (dotted line).

where

$$\delta\phi(\omega) = -\mathrm{Im}\left(\frac{\sum_j \delta s_j s_j^*}{\sum_j s_j s_j^*}\right), \qquad \delta \ln A(\omega) = \mathrm{Re}\left(\frac{\sum_j \delta s_j s_j^*}{\sum_j s_j s_j^*}\right). \tag{4.6}$$

The associated phase and amplitude sensitivity kernels for multitaper measurements are

$$K_\phi^m(\mathbf{x}, \omega) = -\mathrm{Im}\left(\frac{\sum_j \mathcal{K}_j^m(\mathbf{x}, \omega) s_j^*(\omega)}{\sum_j s(\omega) s_j^*(\omega)}\right), \tag{4.7}$$

$$K_A^m(\mathbf{x}, \omega) = \mathrm{Re}\left(\frac{\sum_j \mathcal{K}_j^m(\mathbf{x}, \omega) s_j^*(\omega)}{\sum_j s(\omega) s_j^*(\omega)}\right), \tag{4.8}$$

where

$$\mathcal{K}_j^m(\mathbf{x}, \omega) = \mathcal{K}^m(\mathbf{x}, \omega) \otimes h_j(\omega) \tag{4.9}$$

is the tapered complex waveform kernel. The displacement in the unperturbed earth model, $s(\omega)$, and the complex kernel of the scattered waveform, $\mathcal{K}^m(\mathbf{x}, \omega)$, are given in eqs (2.26) and (2.33).

4.2 Multitaper arrival-angle kernels

The 2×2 spectral density matrix $\mathbf{S}(\omega)$ in the case of a multitaper measurement is a straightforward generalization of eq. (3.12):

$$\mathbf{S}(\omega) = \frac{\sum_j \mathbf{o}_j \mathbf{o}_j^*}{||\sum_j \mathbf{o}_j \mathbf{o}_j^*||}, \tag{4.10}$$

where $\mathbf{o}_j$ are the observed horizontal waveforms tapered with $h_j(t)$:

$$\mathbf{o}_j(\omega) = \mathbf{o}(\omega) \otimes h_j(\omega). \tag{4.11}$$

Due to frequency averaging, the two eigenvalues λ_1 and λ_2 of the matrix $\mathbf{S}(\omega)$ are no longer exactly 1 and 0. However, if the surface wave is reasonably well polarized, it will be the case that $\lambda_1 \approx 1$ and $\lambda_2 \approx 0$, so that the particle motion can still be well approximated by the ellipse associated with the major eigenvector, $\mathbf{o}(t) \approx \mathrm{Re}(\hat{\mathbf{e}}_1 e^{i\omega t})$. In the Born approximation, the multitaper matrix $\mathbf{S}(\omega)$ is given, correct to first order, by

$$\mathbf{S} = \begin{cases} \begin{pmatrix} 0 & \left(\sum_j \delta v_j w_j^*\right)\left(\sum_j w_j w_j^*\right)^{-1} \\ \left(\sum_j w_j \delta v_j^*\right)\left(\sum_j w_j w_j^*\right)^{-1} & 1 \end{pmatrix} & \text{for Love waves,} \\ \begin{pmatrix} 1 & \left(\sum_j v_j \delta w_j^*\right)\left(\sum_j v_j v_j^*\right)^{-1} \\ \left(\sum_j \delta w_j v^*\right)\left(\sum_j v_j v_j^*\right)^{-1} & 0 \end{pmatrix} & \text{for Rayleigh waves,} \end{cases} \tag{4.12}$$

where

$$\begin{aligned} &v_j(\omega) = v(\omega) \otimes h_j(\omega), \quad \delta v_j(\omega) = \delta v(\omega) \otimes h_j(\omega), \\ &w_j(\omega) = w(\omega) \otimes h_j(\omega), \quad \delta w_j(\omega) = \delta w(\omega) \otimes h_j(\omega). \end{aligned} \tag{4.13}$$

eq. (3.19) for the arrival-angle perturbation $\delta\,\xi(\omega)$ is generalized to

$$\delta\xi(\omega) = \begin{cases} -\mathrm{Re}\left[\left(\sum_j \delta v_j w_j^*\right)\left(\sum_j w_j w_j^*\right)^{-1}\right] & \text{for Love waves,} \\ \mathrm{Re}\left[\left(\sum_j \delta w_j v_j^*\right)\left(\sum_j v_j v_j^*\right)^{-1}\right] & \text{for Rayleigh waves.} \end{cases} \tag{4.14}$$

The associated sensitivity kernels for a multitaper arrival-angle measurement are

$$K_\xi^m(\mathbf{x}, \omega) = \begin{cases} -\mathrm{Re}\left[\left(\sum_j \mathcal{V}_j^m(\mathbf{x}, \omega) w_j^*(\omega)\right)\left(\sum_j w_j(\omega) w_j^*(\omega)\right)^{-1}\right] & \text{for Love waves,} \\ \mathrm{Re}\left[\left(\sum_j \mathcal{W}_j^m(\mathbf{x}, \omega) v_j^*(\omega)\right)\left(\sum_j v_j(\omega) v_j^*(\omega)\right)^{-1}\right] & \text{for Rayleigh waves,} \end{cases} \tag{4.15}$$

where

$$\mathcal{V}_j^m(\mathbf{x}, \omega) = \mathcal{V}^m(\mathbf{x}, \omega) \otimes h_j(\omega), \quad \mathcal{W}_j^m(\mathbf{x}, \omega) = \mathcal{W}^m(\mathbf{x}, \omega) \otimes h_j(\omega) \tag{4.16}$$

are the tapered complex horizontal waveform kernels. The expressions for $\mathcal{V}^m(\mathbf{x}, \omega)$ and $\mathcal{W}^m(\mathbf{x}, \omega)$ are given as double sums over σ', σ'' in eq. (2.35), and the expressions for $w(\omega)$ and $v(\omega)$ are given in eq. (2.27). It is straightforward to adapt the sensitivity kernels for multitaper measurements, eqs (4.7), (4.8) and (4.15), to an arbitrary single-taper measurement, by simply dropping the summation over the taper index j.

5 3-D SENSITIVITY KERNELS—EXAMPLES

In this section we present a number of examples of 3-D sensitivity kernels for tapered measurements. The velocity or density heterogeneities (scatterers) are perturbations with respect to a reference model—isotropic PREM with the top water layer replaced by underlying upper crust. The phase, amplitude and arrival-angle sensitivity kernels are computed using eqs (4.7), (4.8) and (4.15). We ignore mode-coupling effects at the outset, i.e. we assume that $\sigma' = \sigma'' = \sigma$; we will discuss the significance of mode coupling in Section 8.

5.1 Minor-arc surface wave kernels

Fig. 4 shows the sensitivity kernels $K_\phi^\beta(\mathbf{x}, \omega)$, $K_A^\beta(\mathbf{x}, \omega)$ and $K_\xi^\beta(\mathbf{x}, \omega)$ for 10 mHz Love waves. The kernels are for measurements made using an 800 s cosine taper, centred at the group arrival time of the 10 mHz fundamental-mode Love wave. The source–receiver epicentral distance is $\Delta = 80^\circ$; the seismic source is a vertical strike-slip fault at a depth of 52 km; Love wave radiation is symmetric with respect to the unperturbed reference ray, and exhibits a maximum in the direction of the reference ray.

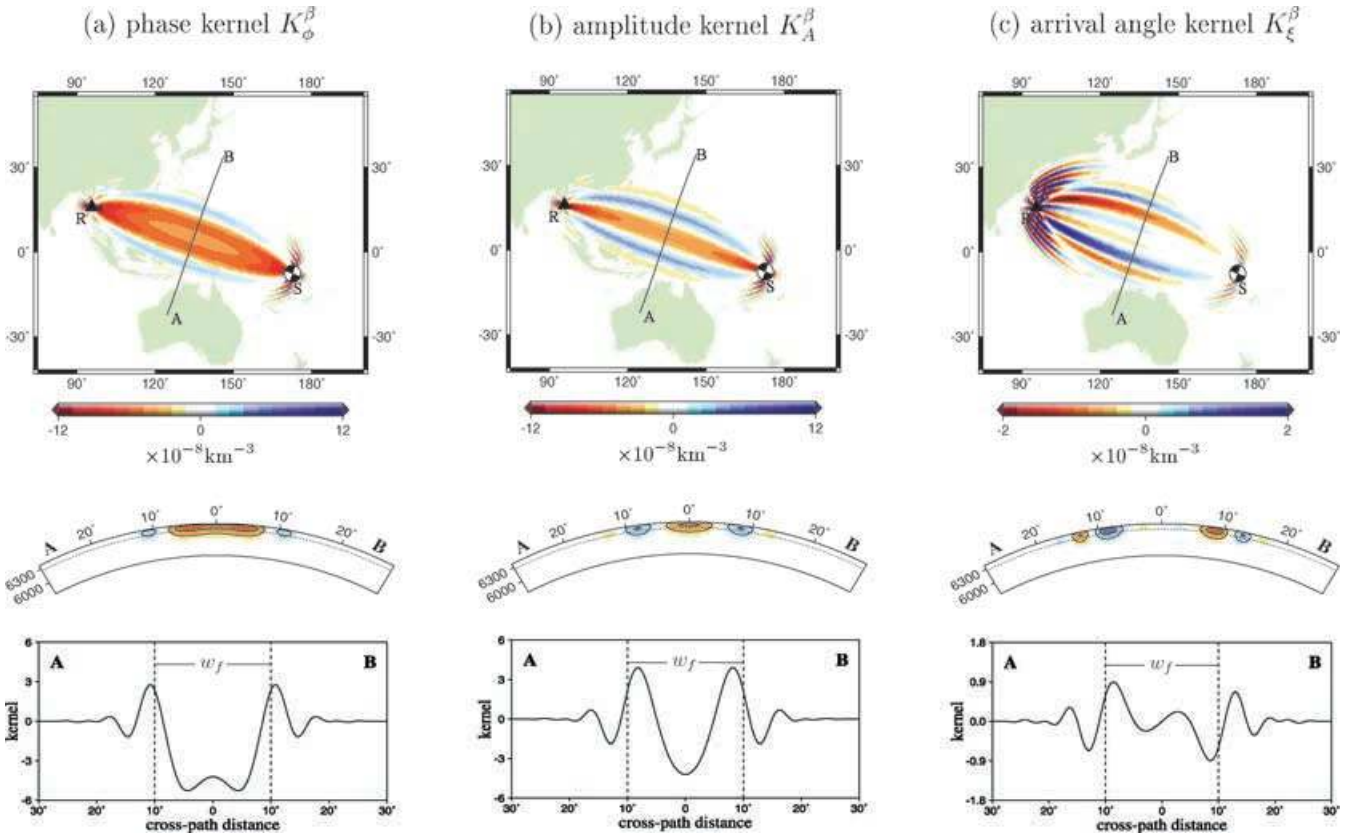

Figure 4. 3-D sensitivity kernels K_ϕ^β, K_A^β, K_ξ^β for a 10 mHz Love wave, excited by a 52 km deep strike-slip seismic source (S). Love wave radiation is maximum in the direction of the source–receiver geometrical ray (see beachball symbol). The epicentral distance to the receiver (R) is $\Delta = 80°$. Sensitivity kernels are for 800 s cosine-taper measurements, with the taper centred at the group arrival time predicted by PREM. Top: Map view of kernels at the depth of approximately greatest sensitivity, 108 km. Middle: Slice view of cross-section AB, dotted lines are plotted at 108 km depth. Bottom: AB cross-section at a depth of 108 km; dashed lines indicate the width of the first Fresnel zone, w_f. Mode-coupling effects have been ignored, i.e. $\sigma_1 = \sigma_2 = \sigma$.

The variation in sensitivity along the source–receiver geometrical ray has a strong-to-weak-to-strong pattern, due to the $(\sin\Delta)^{-1/2}$ geometrical spreading. The cross-sections perpendicular to the reference ray show alternating positive and negative sensitive bands, with an elliptical shape produced by singly scattered waves having the same phase delay. This strong-to-weak-to-strong along-ray variation and the general elliptical character of the sensitivity were accounted for in the recent surface wave tomographic study of Ritzwoller *et al.* (2002). The first Fresnel zone is traditionally defined by

$$k(\Delta' + \Delta'' - \Delta) \leq \pi. \tag{5.1}$$

The width of this region, midway between the source and receiver, is exhibited in Fig. 4. Due to the 2-D propagation nature of surface waves, the on-ray ($\Delta_1 + \Delta_2 - \Delta = 0$) phase of the frequency-dependent oscillatory terms in the kernels is $\pi/4$ rather than zero (Spetzler *et al.* 2002). The region bounded by the zero-sensitivity ellipse (white in Fig. 4a) satisfies

$$k(\Delta' + \Delta'' - \Delta) + \pi/4 \leq \pi. \tag{5.2}$$

This region of strong negative (red) sensitivity is narrower than the first Fresnel zone; negative sensitivity means that a wave is slowed down by a negative shear wave velocity anomaly, $\delta\beta/\beta < 0$, and speeded up by a fast anomaly, $\delta\beta/\beta > 0$. The phase and amplitude sensitivity kernels $K_\phi^m(\mathbf{x}, \omega)$ and $K_A^m(\mathbf{x}, \omega)$ along the source–receiver geometrical ray are neither maximum or zero on the source-to-receiver ray due to the 2-D factor of $\pi/4$ in the phase. This is unlike the 3-D 'banana–doughnut' kernels for the cross-correlation traveltimes of body waves, which exhibit zero traveltime sensitivity and maximal amplitude sensitivity along the geometrical ray (Dahlen *et al.* 2000; Dahlen & Baig 2002). The sensitivity $K_\xi^m(\mathbf{x}, \omega)$ of an arrival-angle measurement is antisymmetric with respect to the reference ray. This is consistent with the arrival-angle perturbation $\delta\xi(\omega)$ being a directional quantity, measured clockwise from the reference ray direction.

The sensitivity beyond the first Fresnel zone decreases rapidly off the geometrical ray (Fig. 4). The decreasing sensitivity is partly due to the weaker source radiation in the off-ray directions, as well as the tapering effects—the oscillatory sidebands are partly cancelled by the destructive interference of adjacent frequencies. The dominant diminution factor in the oscillatory bands is, however, the increasing scattering angle η (Fig. 1) of the far-off-ray scatterers. Scattering becomes inefficient whenever the scattering angle η becomes large. As shown in Fig. 5, the sensitivity kernels computed using a forward-scattering approximation, in which the off-ray scattering angle is approximated by $\eta = 0$, tend to have larger sidebands.

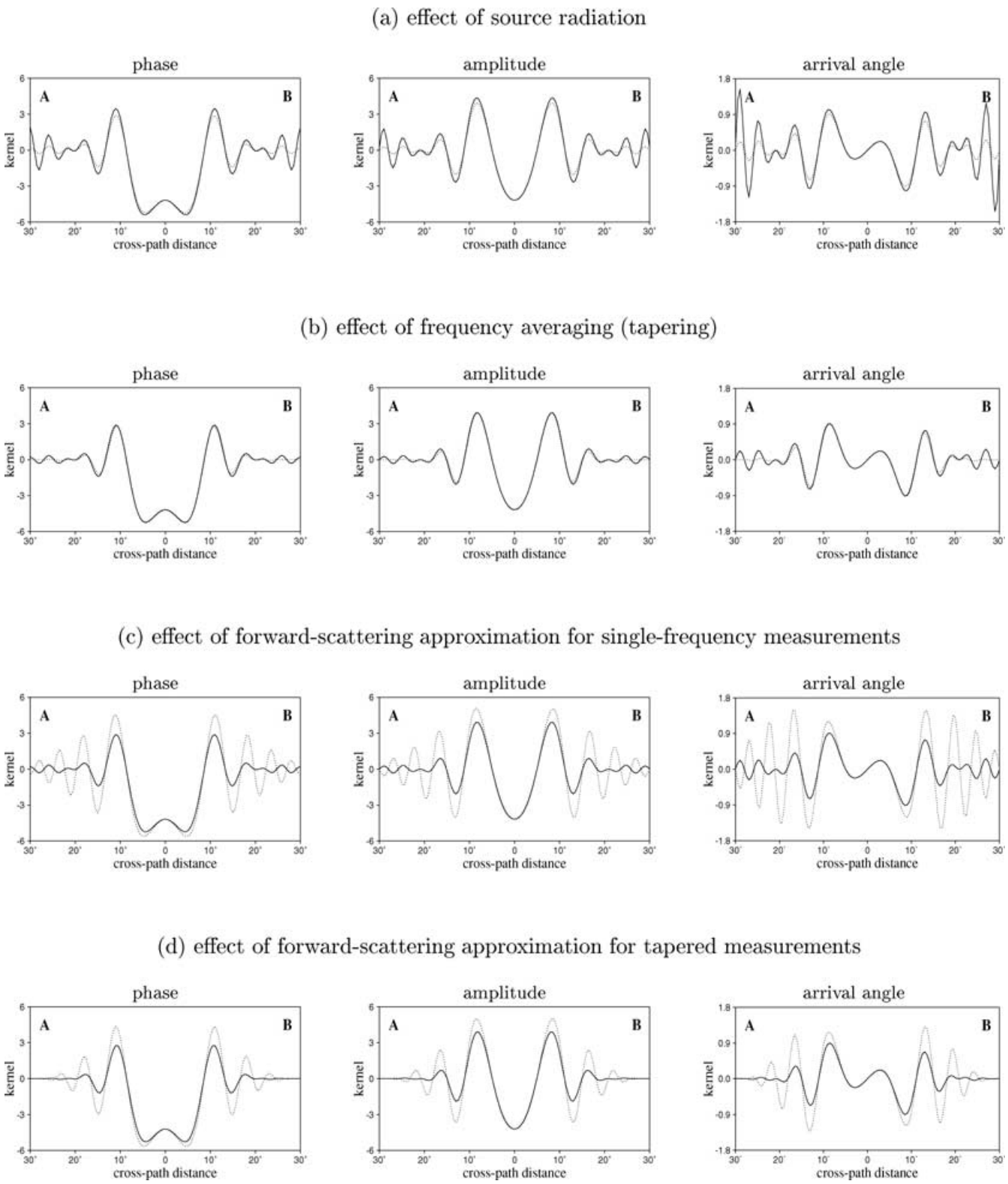

Figure 5. Midpoint AB cross-sections of 10 mHz Love wave sensitivity kernels K_ϕ^β, K_A^β and K_ξ^β, showing the influence of various factors upon the shape of the kernels. The exact 3-D sensitivity kernels are shown in Fig. 4. (a) Effect of source radiation: the solid lines are kernels for an 'artificial' source, with an isotropic Love wave radiation pattern; the dashed lines are kernels for a strike-slip source, with a Love wave radiation pattern that is symmetric with respect to the great-circle ray (same as in Fig. 4). (b) Effect of frequency averaging or tapering: the solid lines are single-frequency sensitivity kernels; the dashed lines are kernels for tapered measurements made using an 800 s cosine taper. (c) The solid lines are the exact sensitivity kernels for single-frequency observables; the dashed lines are single-frequency kernels computed using a forward-scattering approximation in which $\eta = 0$. (d) The solid lines are the exact sensitivity kernels for tapered measurements; the dashed lines are sensitivity kernels for tapered measurements computed using a forward-scattering approximation. Mode-coupling effects have been ignored, i.e. $\sigma_1 = \sigma_2 = \sigma$.

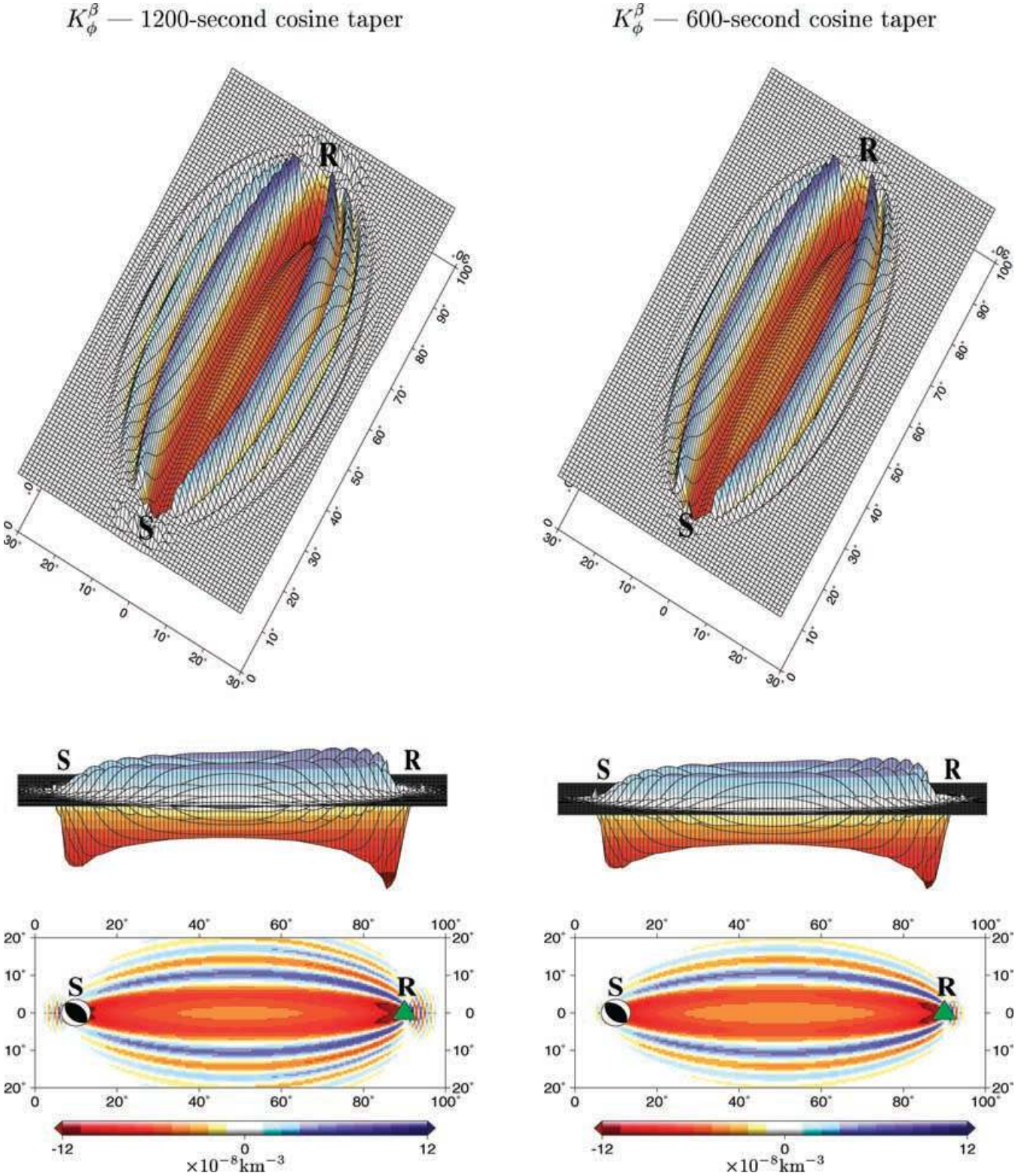

Figure 6. Phase sensitivity kernels K_ϕ^β for 10 mHz Rayleigh wave measurements made on the vertical component using a 1200 s (left) and 600 s (right) cosine taper. All views show the kernels at the depth of approximately maximum sensitivity (108 km). The seismic source is a 45° dip-slip fault at 52 km depth. The Rayleigh wave radiation pattern is symmetric with respect to the source–receiver great-circle ray, and the radiation in the reference ray direction is maximum (see beachball symbol). The oblique perspective views (middle) highlight the enhanced sensitivities near the source (S) and receiver (R). Mode-coupling effects have been ignored, i.e. $\sigma_1 = \sigma_2 = \sigma$.

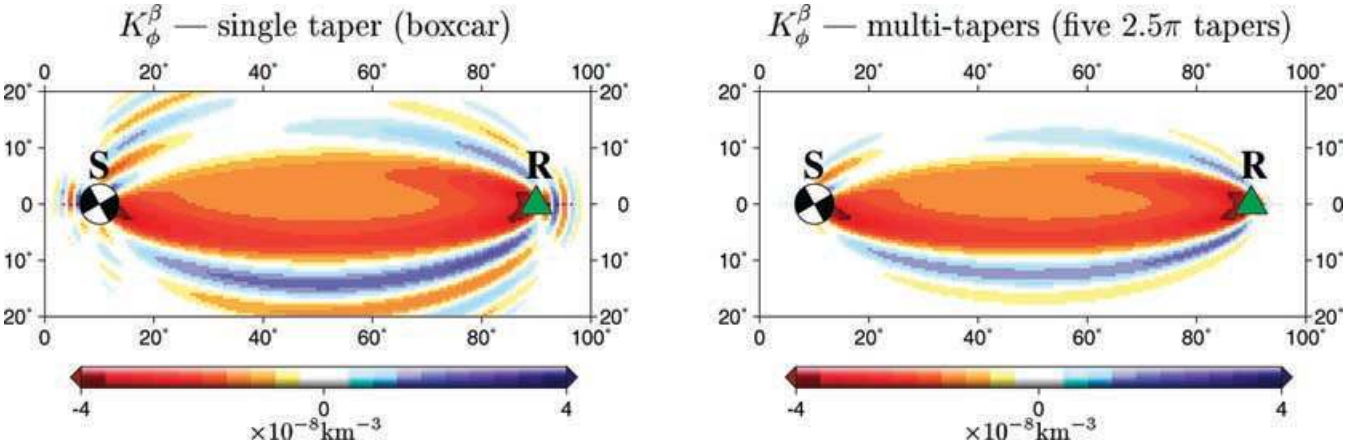

Figure 7. Phase sensitivity kernels K_ϕ^β for 6 mHz Rayleigh waves, measured on the vertical component using an 800 s boxcar taper (left) and the first five 2.5π multitapers (right). The kernels are plotted at the depth of approximately maximum sensitivity, 192 km. The seismic source is a strike-slip fault at 52 km depth. The Rayleigh wave source radiation pattern in this example is non-symmetric with respect to the reference ray, the angle between the maximum radiation and the reference ray in this example is 15°.

The spatial extent of the oscillatory sidebands in the sensitivity kernels is significantly affected by the length of the taper used in making the measurements. The uncertainty principle guarantees that a shorter time-domain window has a wider spectral content; therefore, the sensitivity kernels for measurements made using a shorter window involve more frequency averaging, and thereby more effective cancellation of the oscillatory sidebands. It is not surprising that a shorter time-domain window picks up less scattered energy. In Fig. 6, we compare 10 mHz Rayleigh wave sensitivity kernels $K_\phi^\beta(\mathbf{x}, \omega)$ for phase delays made using cosine tapers of different length. The sensitivity kernel for a 1200 s cosine-taper measurement shows stronger sidebands than the kernel for a 600 s cosine-taper measurement. In practice, Rayleigh waves are often measured using longer windows than Love waves, due to their more dispersed nature. Therefore, the sensitivity kernels for Rayleigh wave measurements may contain more oscillatory sidebands. The 3-D geometry of the sensitivity kernels is also affected by the spectral property of the tapers. Fig. 7 illustrates the sensitivity kernel $K_\phi^\beta(\mathbf{x}, \omega)$ for multitaper measurements and for boxcar measurements. The sensitivity kernel for the boxcar measurement shows stronger sidebands. Notice that neither sensitivity kernel in Fig. 7 is symmetric with respect to the reference ray, because of the non-symmetric source radiation.

In conclusion, Figs 5–7 show that the detailed shape of the kernels depends upon the details of the measurement process, and whether or not effects such as the source radiation pattern are taken into account in the theoretical analysis. By and large, however, it is the sideband structure of the kernels that is most strongly affected by these considerations; within the first Fresnel zone, all of the kernels are more or less the same.

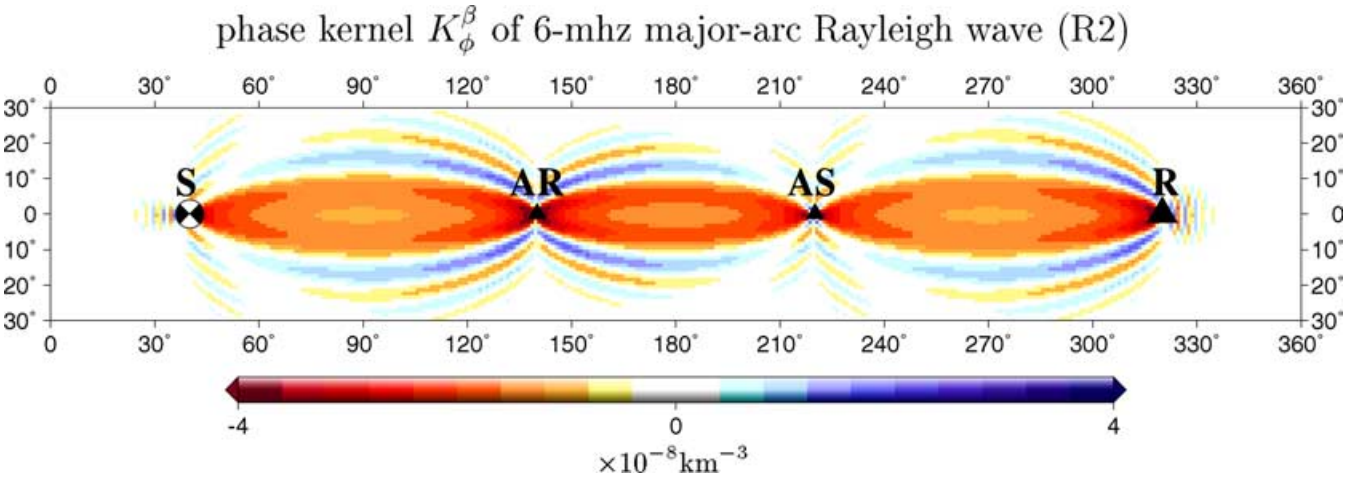

Figure 8. Phase sensitivity kernel K_ϕ^β for major-arc Rayleigh waves (R2) at a frequency of 6 mHz, plotted at a depth of 192 km. The seismic source is a strike-slip fault (see beachball symbol) at 11 km depth. The receiver epicentral distance is $\Delta = 80°$. The Rayleigh wave radiation pattern is symmetric with respect to the source–receiver great-circle direction, and maximum along the great-circle ray. The phase kernel is for vertical-component measurements made using a 3280 s cosine taper, centred at the group arrival time predicted by PREM. Mode-coupling effects have been ignored, i.e. $\sigma_1 = \sigma_2 = \sigma$.

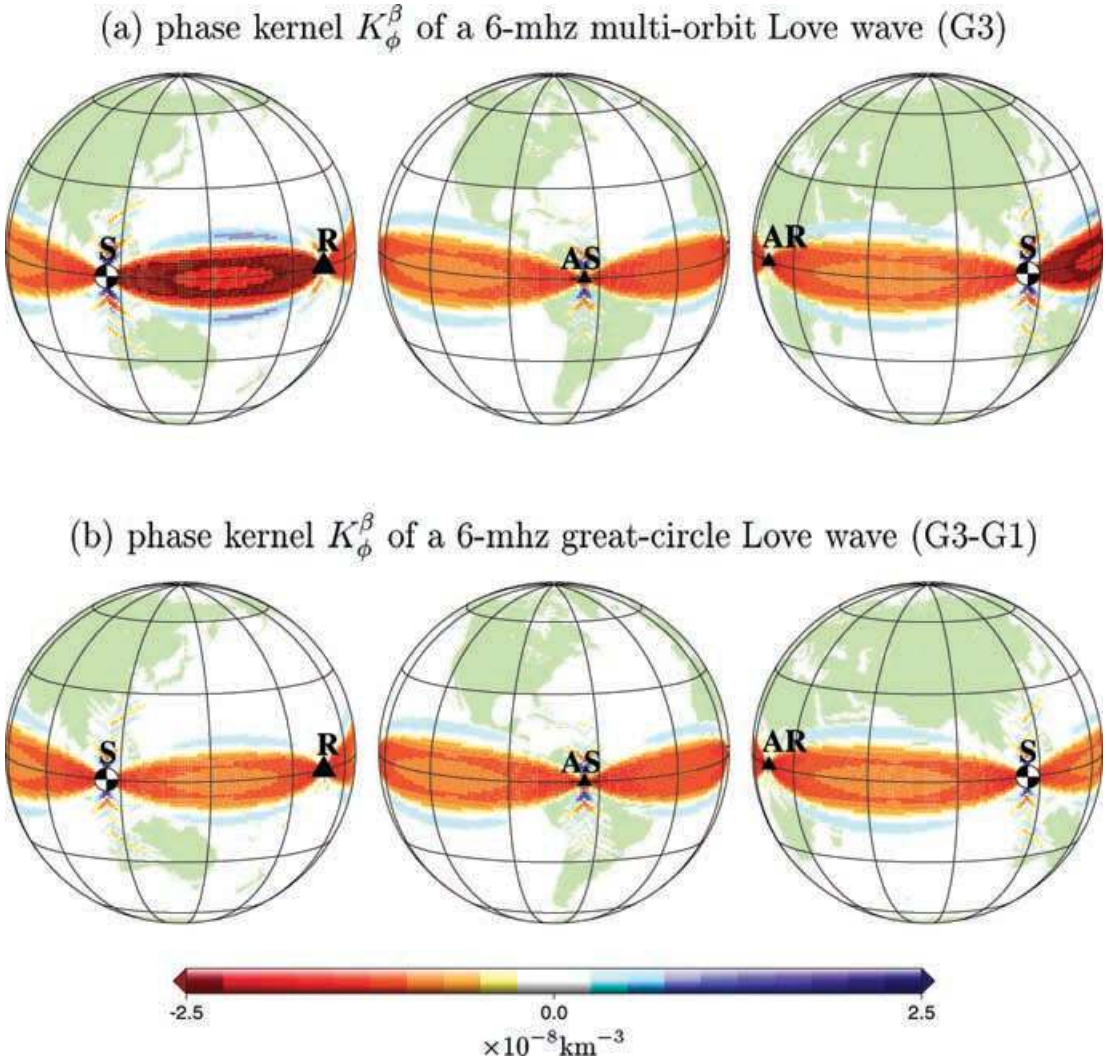

Figure 9. (a) Phase sensitivity kernel K_ϕ^β for a multi-orbit Love wave (G3) at a frequency of 6 mHz. (b) Phase sensitivity kernel K_ϕ^β for a great-circle Love wave (G3–G1) measurement at the same frequency, 6 mHz. Both kernels are plotted at a depth of 220 km. The seismic source is a strike-slip source (see beachball symbol) at 11 km depth. The receiver epicentral distance is $\Delta = 80^\circ$. Love wave radiation is symmetric with respect to the source–receiver great-circle ray, and maximum along the great-circle ray. The Love wave sensitivity kernels are for transverse-component measurements made using a cosine taper, centred at the group arrival time predicted by PREM. The length of the taper is 1640 s for the G3 wave train and 800 s for the G1 wave train. Mode-coupling effects are not included, i.e. $\sigma_1 = \sigma_2 = \sigma$.

5.2 Major-arc, multi-orbit and great-circle paths

In global surface wave tomography measurements are often made for major-arc and multi-orbit wave trains, in addition to minor-arc paths, in order to improve the geographical coverage. Due to the spherical geometry of the Earth, the antipodes of the source and receiver play a critical role in the surface wave propagation. Fig. 8 shows the sensitivity kernel $K_\phi^\beta(\mathbf{x}, \omega)$ for a major-arc Rayleigh wave (R2) at a frequency of 6 mHz. In map view, the sensitivity resembles a sausage link, with 'pinches' at the source and receiver antipodes (AS and AR). This antipodal 'pinching' has been noted previously by Wang & Dahlen (1995) and Spetzler *et al.* (2002). Fig. 9 shows the sensitivity kernel $K_\phi^\beta(\mathbf{x}, \omega)$ of a multi-orbit Love wave (G3) at a frequency of 6 mHz. The G3 wave train samples the source–receiver minor arc twice, so that it has a doubled sensitivity in this region. Due to the linearity, the sensitivity kernel for any differential measurement is simply the difference between the sensitivity kernels for the individual measurements. For example, the sensitivity kernel of a great-circle G3–G1 measurement is

$$K_d^m(\mathbf{x}, \omega)_{\mathrm{G3–G1}} = K_d^m(\mathbf{x}, \omega)_{\mathrm{G3}} - K_d^m(\mathbf{x}, \omega)_{\mathrm{G1}}. \tag{5.3}$$

In regions near the source, receiver or their antipodes, scattered waves which take paths far from the great circle may arrive at the receiver within the measurement window for the major-arc or multi-orbit wave trains. We have done experiments which have convinced us that these Earth-covering paths only affect the sensitivity within a very small region around the source, receiver and their antipodes, and the effect itself is relatively small. Therefore, only the near-great-circle paths are included in our calculation.

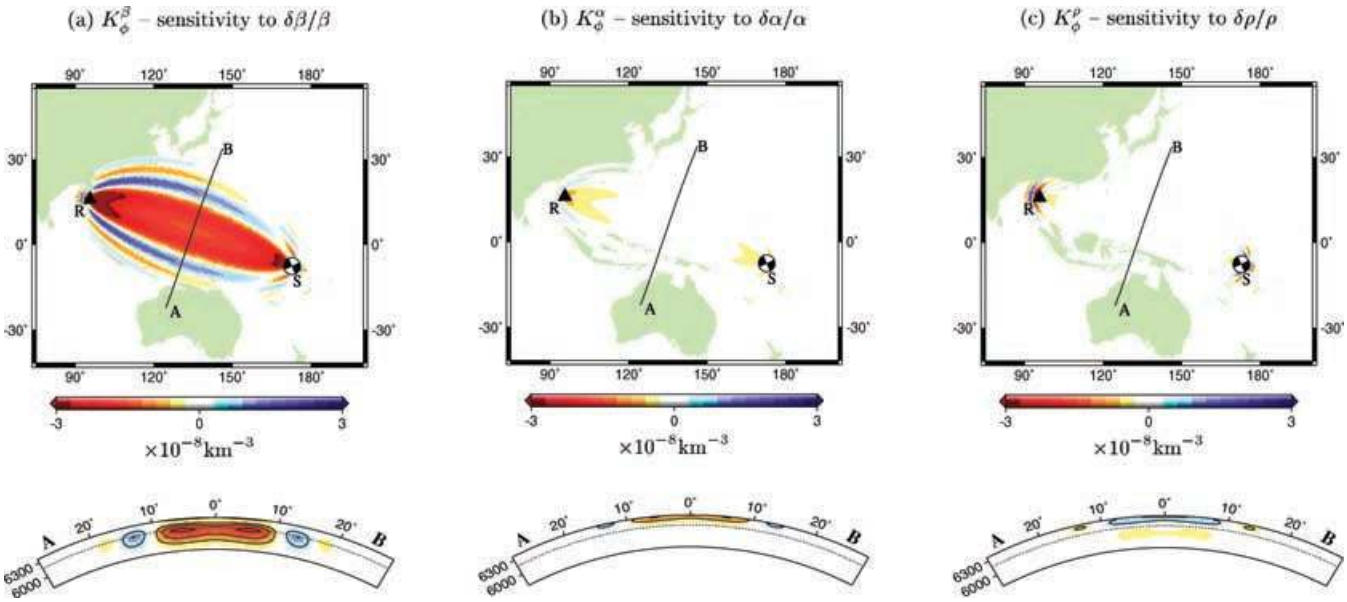

Figure 10. 3-D sensitivity kernels K_ϕ^β, K_ϕ^α, K_ϕ^ρ for 6 mHz Rayleigh waves. Top: Map views of the kernels at a depth of 192 km. Bottom: Slice views of the AB cross-sections. The dashed lines are plotted at a constant depth of 192 km for reference. The seismic source is a strike-slip fault at 7 km depth (see beachball symbol). The Rayleigh wave radiation pattern is symmetric with respect to the great-circle ray, and maximum along the great-circle ray. The receiver epicentral distance is $\Delta = 80^\circ$. The sensitivity kernels are for vertical-component measurements made using an 800 s cosine taper, centred at the group arrival time predicted by PREM. Mode-coupling effects are not included, i.e. $\sigma_1 = \sigma_2 = \sigma$.

5.3 Sensitivity to compressional wave velocity and density perturbations

In Fig. 10, we compare $K_\phi^\beta(\mathbf{x}, \omega)$, $K_\phi^\alpha(\mathbf{x}, \omega)$ and $K_\phi^\rho(\mathbf{x}, \omega)$, the phase-delay sensitivities to a fractional shear wave velocity perturbation $\delta\beta/\beta$, a fractional compressional wave perturbation $\delta\alpha/\alpha$, and a fractional density perturbation $\delta\rho/\rho$. The sensitivity kernels are computed for 6 mHz Rayleigh waves, assuming an 800 s measurement window and a cosine taper. As is well known, $K_\phi^\beta(\mathbf{x}, \omega)$ is much stronger than either $K_\phi^\alpha(\mathbf{x}, \omega)$ or $K_\phi^\rho(\mathbf{x}, \omega)$, i.e. the surface waves are mostly sensitive to shear wave velocity perturbations. A Love wave has no sensitivity whatsoever to a compressional wave speed perturbation; for Rayleigh waves, the sensitivity kernel $K_\phi^\alpha(\mathbf{x}, \omega)$ is not zero, but it is very weak and confined to relatively shallow depths. The sensitivity $K_\phi^\rho(\mathbf{x}, \omega)$ to a density perturbation shows a polarity change at a depth of about a quarter of a wavelength. In 3-D surface wave tomography, it is reasonable to focus our primary attention upon the sensitivity to shear wave velocity perturbations $\delta\beta/\beta$.

6 REDUCTION TO 2-D SENSITIVITY KERNELS

We show next that kernels $K_d^{\alpha,\beta,\rho}(\mathbf{x}, \omega)$, expressing the sensitivities to 3-D perturbations in density $\delta\rho/\rho$, shear wave speed $\delta\beta/\beta$ and compressional wave speed $\delta\alpha/\alpha$, can be combined to find the 2-D sensitivity to the local phase-velocity perturbation, $\delta c/c$, using a forward-scattering approximation. The 2-D sensitivity kernel $K_d^c(\hat{\mathbf{r}}, \omega)$ is defined as

$$\delta d(\omega) = \int\int_\Omega K_d^c(\hat{\mathbf{r}}, \omega) \left(\frac{\delta c}{c}\right) d\Omega, \tag{6.1}$$

where the integration is over the unit sphere $\Omega = \{\hat{\mathbf{r}} : ||\hat{\mathbf{r}}||^2 = 1\}$. In the expressions for the single-frequency 3-D sensitivity kernels (3.9), (3.10) and (3.20); the only depth-dependent term is the scattering coefficient ${}_{\sigma'}\Omega^m_{\sigma''}$. If we neglect mode-coupling effects, i.e. assume that $\sigma' = \sigma'' = \sigma$, and make the forward-scattering approximation $\eta = \arccos(\mathbf{k}' \cdot \mathbf{k}'') = 0$, the integration over depth can be performed analytically:

$$\int_0^a \left[{}_{\sigma'}\Omega^\alpha_{\sigma''} \left(\frac{\delta\alpha}{\alpha}\right) + {}_{\sigma'}\Omega^\beta_{\sigma''} \left(\frac{\delta\beta}{\beta}\right) + {}_{\sigma'}\Omega^\rho_{\sigma''} \left(\frac{\delta\rho}{\rho}\right) \right] r^2 \quad dr = -2k^2 \left(\frac{\delta c}{c}\right), \tag{6.2}$$

where $c = \omega/k$ is the phase velocity measured in rad s^{-1}, and where $\delta c(\hat{\mathbf{r}}, \omega)$ is the associated local perturbation in phase velocity. The resulting 2-D sensitivity kernels $K_d^c(\hat{\mathbf{r}}, \omega)$ are:

$$K_\phi^c(\hat{\mathbf{r}}, \omega) = \mathrm{Im}\left(\frac{2k^2 \mathcal{S}'\mathcal{R}'' \mathrm{e}^{-i[k(\Delta' + \Delta'' - \Delta) - (n' + n'' - n)\pi/2 + \pi/4]}}{\mathcal{S}\mathcal{R}\sqrt{8\pi k(|\sin\Delta'||\sin\Delta''|/|\sin\Delta|)}} \right), \tag{6.3}$$

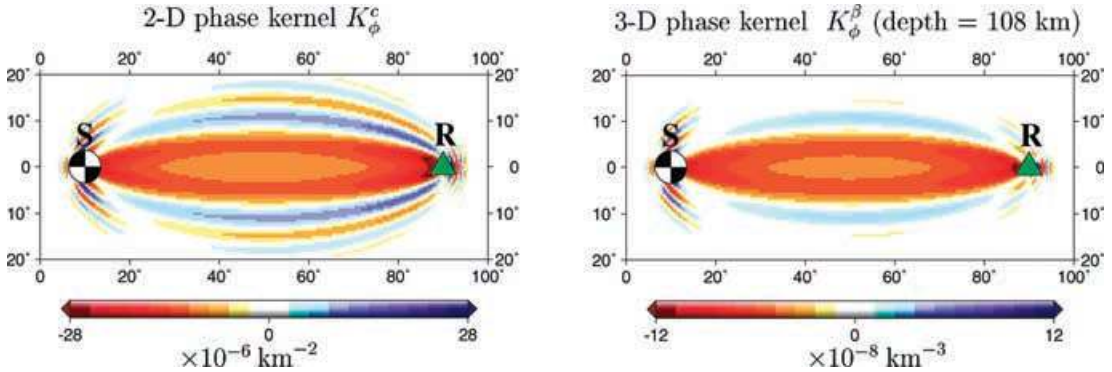

Figure 11. 2-D phase kernel K_ϕ^c (left) and 3-D phase kernel K_ϕ^β (right) for a 10 mHz Love wave. The 3-D kernel is plotted at a depth of 108 km. Both kernels are for measurements made using an 800 s cosine taper. The seismic source is a strike-slip fault at 52 km depth, the source–receiver epicentral distance is $\Delta = 80^\circ$. Love wave source radiation is symmetric with respect to the source–receiver great-circle direction and maximum along the great-circle ray (see beachball symbol). Mode-coupling effects have been ignored, i.e. $\sigma_1 = \sigma_2 = \sigma$.

$$K_A^c(\hat{\mathbf{r}}, \omega) = -\mathrm{Re}\left(\frac{2k^2\mathcal{S}'\mathcal{R}''\mathrm{e}^{-i[k(\Delta'+\Delta''-\Delta)-(n'+n''-n)\pi/2+\pi/4]}}{\mathcal{S}\mathcal{R}\sqrt{8\pi k(|\sin\Delta'||\sin\Delta''|/|\sin\Delta|)}}\right), \tag{6.4}$$

$$K_\xi^c(\hat{\mathbf{r}}, \omega) = -\mathrm{Re}\left(\frac{2k^2\mathcal{S}'\sin(\xi''-\xi)\mathrm{e}^{-i[k(\Delta'+\Delta''-\Delta)-(n'+n''-n)\pi/2+\pi/4]}}{\mathcal{S}\sqrt{8\pi k(|\sin\Delta'||\sin\Delta''|/|\sin\Delta|)}}\right). \tag{6.5}$$

Fig. 11 compares the 2-D sensitivity kernel $K_\phi^c(\hat{\mathbf{r}}, \omega)$ for a 10 mHz Love wave with the associated 3-D kernel sensitivity $K_\phi^\beta(\mathbf{x}, \omega)$ at a depth of 108 km. The 2-D sensitivity kernel $K_\phi^c(\hat{\mathbf{r}}, \omega)$ exhibits slightly stronger sidebands, as a result of the forward-scattering approximation.

7 REDUCTION TO RAY THEORY

7.1 Analytical verification

We show next that the 2-D sensitivity kernels in eqs (6.3)–(6.5) can be further reduced to 1-D ray theoretical predictions (Woodhouse & Wong 1986), provided that the heterogeneities vary slowly over space so that the sizes of the anomalies are much larger than the width of the Fresnel zone. For brevity, we exhibit the reduction to ray theory only for the minor-arc wave, with polar passage indices $n' = n'' = n = 0$. We neglect the effects of the source radiation pattern; i.e. we assume that $\mathcal{S}' \approx \mathcal{S}$. For the phase and amplitude kernels, we also neglect the difference in the arrival angle of the direct and scattered waves by assuming that $\mathcal{R}'' \approx \mathcal{R}$; for the arrival-angle kernel, we make the next highest-order approximation

$$\mathcal{R}''/\mathcal{R} = \sin(\xi''-\xi) \approx -y/\sin(\Delta - x), \tag{7.1}$$

where x is the source–scatterer distance projected onto the unperturbed ray, and y is the perpendicular distance from the scatterer to the reference ray (see Fig. 1). In addition, we make the following geometrical simplifications:

$$|\sin\Delta'||\sin\Delta''| \approx \sin x \sin(\Delta - x), \tag{7.2}$$

$$\Delta' + \Delta'' - \Delta \approx \frac{1}{2}\Gamma y^2 \quad \text{where} \quad \Gamma = \sin\Delta/[\sin x \sin(\Delta - x)]. \tag{7.3}$$

The simplified 2-D sensitivity kernels in this paraxial, forward-scattering approximation are

$$K_\phi^c(x, y, \omega) = -\sqrt{\frac{k^3\Gamma}{2\pi}}\sin\left(\frac{1}{2}k\Gamma y^2 + \pi/4\right), \tag{7.4}$$

$$K_A^c(x, y, \omega) = \sqrt{\frac{k^3\Gamma}{2\pi}}\cos\left(\frac{1}{2}k\Gamma y^2 + \pi/4\right), \tag{7.5}$$

$$K_\xi^c(x, y, \omega) = \sqrt{\frac{k^3\Gamma}{2\pi}}\left(\frac{y}{\sin(\Delta - x)}\right)\cos\left(\frac{1}{2}k\Gamma y^2 + \pi/4\right). \tag{7.6}$$

The kernel K_ϕ^c in eq. (7.4) has been given previously by Spetzler *et al.* (2002). Assuming that the size of the anomaly is much larger than the width of the Fresnel zone, so that the anomaly varies smoothly over space, we make use of a similarly limited expansion of the anomaly field $\delta c(x, y)$ around the reference ray. For the phase delay $\delta\phi(\omega)$, we need only expand $\delta c(x, y)$ to zeroth order:

$$\delta c(x, y) \approx \delta c(x, 0), \tag{7.7}$$

and make use of eq. (7.4):

$$\begin{aligned}\delta\phi(\omega) &= \frac{1}{c}\int\int_{\Omega} K_\phi^c(x, y, \omega)\delta c(x, y)\, d\Omega \\ &\approx \frac{1}{c}\int_0^\Delta \delta c(x, 0)\, dx \int_{-\infty}^{\infty} K_\phi^c(x, y, \omega)\, dy \\ &= -\frac{k}{c}\int_0^\Delta \delta c(x, 0)\, dx.\end{aligned} \tag{7.8}$$

For the arrival-angle perturbation $\delta\xi(\omega)$ we expand the perturbation field $\delta c(x, y)$ to first order,

$$\delta c(x, y) \approx \delta c(x, 0) + y\partial_y \delta c(x, 0), \tag{7.9}$$

and make use of eq. (7.6):

$$\begin{aligned}\delta\xi(\omega) &= \frac{1}{c}\int\int_{\Omega} K_\xi^c(x, y, \omega)\delta c(x, y)\, d\Omega \\ &\approx \frac{1}{c}\int_0^\Delta \delta c(x, 0) dx \int_{-\infty}^{\infty} K_\xi^c(x, y, \omega)\, dy \\ &\quad + \frac{1}{c}\int_0^\Delta \partial_y \delta c(x, 0) dx \int_{-\infty}^{\infty} y K_\xi^c(x, y, \omega)\, dy \\ &= -\frac{1}{c\sin\Delta}\int_0^\Delta \sin x\, \partial_y \delta c(x, 0)\, dx.\end{aligned} \tag{7.10}$$

For the amplitude variations $\delta \ln A\,(\omega)$ we expand the perturbation field $\delta c(x, y)$ to second order,

$$\delta c(x, y) \approx \delta c(x, 0) + y\partial_y \delta c(x, 0) + \frac{1}{2}y^2\partial_y^2 \delta c(x, 0), \tag{7.11}$$

and make use of eq. (7.5):

$$\begin{aligned}\delta \ln A(\omega) &= \frac{1}{c}\int\int_{\Omega} K_A^c(x, y, \omega)\delta c(x, y)\, d\Omega \\ &\approx \frac{1}{c}\int_0^\Delta \delta c(x, 0) dx \int_{-\infty}^{\infty} K_A^c(x, y, \omega)\, dy \\ &\quad + \frac{1}{c}\int_0^\Delta \partial_y \delta c(x, 0) dx \int_{-\infty}^{\infty} y K_A^c(x, y, \omega)\, dy \\ &\quad + \frac{1}{2c}\int_0^\Delta \partial_y^2 \delta c(x, 0) dx \int_{-\infty}^{\infty} y^2 K_A^c(x, y, \omega)\, dy \\ &= \frac{1}{2c\sin\Delta}\int_0^\Delta \sin(\Delta - x)\sin x\, \partial_y^2 \delta c(x, 0)\, dx.\end{aligned} \tag{7.12}$$

In deriving eqs (7.8), (7.10) and (7.12) we have made use of the identities

$$\begin{aligned}&\int_{-\infty}^{\infty} \cos\left(\frac{1}{2}k\Gamma y^2 + \frac{\pi}{4}\right) dy = 0, \qquad \int_{-\infty}^{\infty} y\cos\left(\frac{1}{2}k\Gamma y^2 + \frac{\pi}{4}\right) dy = 0, \\ &\int_{-\infty}^{\infty} \sin\left(\frac{1}{2}k\Gamma y^2 + \frac{\pi}{4}\right) dy = \sqrt{\frac{2\pi}{k\Gamma}}, \qquad \int_{-\infty}^{\infty} y^2\cos\left(\frac{1}{2}k\Gamma y^2 + \frac{\pi}{4}\right) dy = -\sqrt{\frac{2\pi}{k\Gamma}}\frac{1}{k\Gamma}.\end{aligned} \tag{7.13}$$

In the above expressions for the 1-D sensitivity kernels, the phase delay $\delta\phi(\omega)$ depends upon the phase-velocity perturbation along the ray, $\delta c(x, 0)$; the arrival-angle perturbation $\delta\xi(\omega)$ depends upon the first derivative of the phase-velocity perturbation in the direction perpendicular to the unperturbed ray, $\partial_y \delta c(x, 0)$; and the amplitude variation $\delta \ln A(\omega)$ depends upon the second cross-path derivative, ∂_y^2 $\delta c(x, 0)$. Eqs (7.8) and (7.10) coincide precisely with the the *ab initio* ray-theoretical predictions, and eq. (7.12) is the dominant term in the ray-theoretical amplitude (Woodhouse & Wong 1986; Dahlen & Tromp 1998, Sections 16.8.4–16.8.5). The above analysis shows that they are recovered in the limit of a sufficiently smooth heterogeneity.

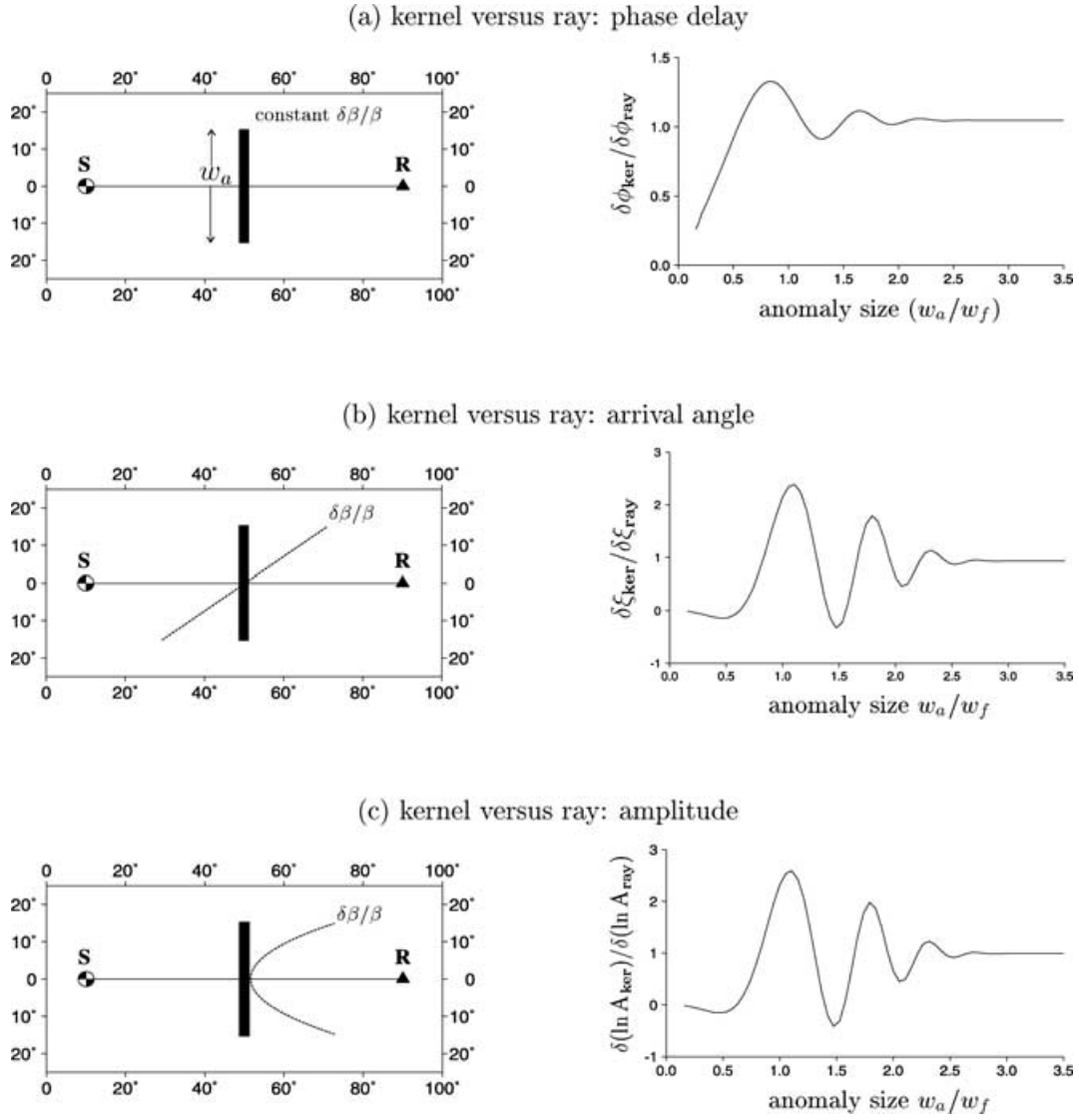

Figure 12. Numerical illustration of the reduction of the 3-D sensitivity to ray theory as the size of the anomaly increases; all examples are for 10 Hz Rayleigh waves. Left: Geometry of the anomalies in this experiment: the velocity perturbation $\delta\beta/\beta$ does not vary with longitude; the anomalies are 2° in length, and the width $w_{\rm a}$ is allowed to vary; the anomalies extend in depth throughout the sensitivity region of the 10 mHz Rayleigh waves. (a) The velocity perturbation $\delta\beta/\beta$ is constant. (b) $\delta\beta/\beta$ has a constant first derivative perpendicular to the reference ray. (c) $\delta\beta/\beta$ has a constant second derivative perpendicular to the reference ray. The magnitude of $\delta\beta/\beta$ in all three examples is irrelevant, since we are simply comparing two linear theories. Right: Ratio of the observables $\delta d_{\rm ker}/\delta d_{\rm ray}$ plotted as a function of $w_{\rm a}/w_{\rm f}$, the width of the anomaly $w_{\rm a}$ normalized by the width of the first Fresnel zone $w_{\rm f}$. The ratios of $\delta\phi_{\rm ker}/\delta\phi_{\rm ray}$, $\delta\xi_{\rm ker}/\delta\xi_{\rm ray}$ and $\delta\ln A_{\rm ker}/\delta\ln A_{\rm ray}$ converge to unity as the normalized anomaly size, $w_{\rm a}/w_{\rm f}$, increases.

7.2 Numerical illustration

In this section, we provide a numerical illustration of the fact that the 3-D sensitivity kernels based upon the Born approximation converge to ray theory whenever the anomaly size is much larger than the width of the first Fresnel zone. We compare the kernel predictions and the ray-theoretical predictions for phase delays $\delta\phi(\omega)$, amplitude variations $\delta\ln A(\omega)$ and arrival-angle perturbations $\delta\xi(\omega)$, as the size of the anomaly $w_{\rm a}$ varies. As shown in Fig. 12, the anomaly is a narrow band crossing the ray path midway between the source and receiver, and extending in depth well below the region of negligible sensitivity. The along-ray length of the anomaly is 2°, and the cross-ray width, $w_{\rm a}$, is allowed to vary. We use eqs (3.9), (3.10) and (3.20) to compute the 3-D sensitivity kernels; and eqs (3.8) and (3.11) to compute the phase delays $\delta\phi(\omega)$, amplitude variation $\delta\ln A(\omega)$ and the arrival-angle perturbations $\delta\xi(\omega)$ due to the anomalies. The ray-theoretical predictions of the same quantities are computed using eqs (7.8), (7.10) and (7.12). All computations are carried out for a 10 mHz Rayleigh wave. The source–receiver epicentral distance is 80°; the source radiation is symmetric and is maximum in the reference ray direction. In Fig. 12, we plot the kernel-to-ray ratios of the predicted phase delays (amplitude variations, arrival-angle perturbations) as a function of the normalized anomaly size $w_{\rm a}/w_{\rm f}$, where $w_{\rm f}$ is the width of the first Fresnel zone, calculated using eq. (5.1). As the size ratio $w_{\rm a}/w_{\rm f}$ increases, the kernel-to-ray ratios $\delta\phi_{\rm ker}/\delta\phi_{\rm ray}$, $\delta\xi_{\rm ker}/\delta\xi_{\rm ray}$ and $\delta\ln A_{\rm ker}/\delta\ln A_{\rm ray}$ all approach unity. In general, the phase-delay ratios $\delta\phi_{\rm ker}/\delta\phi_{\rm ray}$ converge faster than the ratios of arrival angle and amplitude, $\delta\xi_{\rm ker}/\delta\xi_{\rm ray}$ and $\delta\ln A_{\rm ker}/\delta\ln A_{\rm ray}$.

8 MODE COUPLING AND RESOLUTION

So far, in our illustrative examples we have ignored surface wave mode-coupling effects, by assuming that $\sigma' = \sigma'' = \sigma$. In this section, we shall investigate the significance of surface wave mode-coupling effects in fundamental-mode surface wave measurements.

8.1 Mode-coupling effects on phase kernels

Fig. 13 displays examples of sensitivity kernels computed with and without taking into account mode-coupling effects. In the top panel, the 6 mHz Rayleigh waves are excited by a non-symmetric seismic source; the angle between the maximum Rayleigh wave radiation and the reference ray is 15°. The sensitivity is zero along the Rayleigh wave excitation nodal plane when mode coupling is not taken into account (left). However, the 'nodal panel' in the sensitivity kernel $K_\phi^\beta(\mathbf{x}, \omega)$ is filled up once mode-coupling effects are taken into account (right). This is because Love-to-Rayleigh scattering is now accounted for, and the Love wave radiation is maximum in the Rayleigh wave nodal plane. Waves leaving the source as Love waves and arriving at the receiver as scattered Rayleigh waves now contribute to the sensitivity. Coupling between like-type higher modes and the fundamental mode is better illustrated when the source radiation is symmetric with respect to the reference ray. The Love wave sensitivity kernels in the second-from-top panel in Fig. 13 show the effects of higher Love modes. The seismic source in this case is a strike-slip source, and the Love wave radiation is maximum in the direction of the reference ray; therefore, Rayleigh-to-Love scattering is nearly negligible and the coupling between the Love wave overtones and the fundamental-mode Love wave is highlighted. The coupling gives rise to significant variations in the sensitivity along the great-circle ray. In all cases where mode coupling is considered, we include all possible surface wave modes at the frequency of interest (12 Rayleigh wave modes and five Love wave modes for the 6 mHz waves in Fig. 13).

8.2 Coarse parametrization effects

Phase sensitivity kernels calculated with and without mode coupling can look quite different in their details. In regional tomography, where the data may be adequate to resolve small-scale structures, the incorporation of mode coupling is important to map the 3-D anomalies accurately in space. Small-scale features, such as the detailed geometry of a subduction zone, can also be resolved in global surface wave tomography if the data coverage is sufficient. In these cases, it may be necessary to account for mode coupling in constructing the sensitivity kernels. On the other hand, in global tomography the desired resolution based on available data may not require full knowledge of the small-scale details of the sensitivity, but only the average sensitivity in coarsely parametrized blocks or voxels. To simulate a coarse volumetric parametrization, the sensitivity kernels in the top two panels in Fig. 13 have been averaged over a circular cap with a radius of 6°, and plotted in the bottom two panels. The difference between the sensitivity kernels computed with and without mode coupling is significantly reduced by this cap averaging.

Quantitative experiments on mode-coupling effects are shown in Fig. 14, for the case of 6 mHz Rayleigh-wave phase-delay sensitivity kernels $K_\phi^\beta(\mathbf{x}, \omega)$, computed with and without mode coupling. The anomaly in each experiment has a fixed size, but a variable position along (or parallel to) the reference ray. We compute the phase delay $\delta\phi(\omega)$ as the anomaly moves, both with (triangle) and without (diamond) mode-coupling effects taken into account. For anomalies centred on the ray, mode-coupling effects are significant whenever the anomalies are close to the source or to the receiver. If an anomaly is completely off the reference ray, mode coupling effects can be considerable; however, the overall phase delay due to a completely off-ray anomaly is relatively small.

8.3 Mode-coupling effects on arrival-angle kernels

Figs 15(a) and 15(b) show strong mode-coupling effects on arrival-angle measurements. The sensitivity kernels are for the arrival-angle perturbations of 6 mHz Love waves, measured using a 400 s cosine taper. The position of the taper is indicated by the dashed lines in Fig. 15(f). The difference in the sensitivity kernels due to mode coupling is reduced when the sensitivity kernels are averaged over a circular cap with a radius of 6°. However, the difference is still considerable in these cap-averaged sensitivity kernels (Figs 15c and d). Figs 15(g) and 15(f) are examples of perturbed horizontal-component seismograms computed without and with accounting for the effects of mode coupling, assuming an off-ray cylindrical anomaly (Fig. 15e). The seismograms are bandpass filtered; the filter response is flat between 4 and 6 mHz, and tapers off to zero at the ends, 0 and 10 mHz. The seismograms computed with and without mode coupling are significantly different. We should point out that the shear wave velocity perturbation in this example is −50 per cent, which is unrealistically high. Such a strong single anomaly is required for illustration purposes, in order to highlight the effects of mode coupling in the bandpass-filtered seismograms.

9 FAST KERNEL COMPUTATION

Computation of the exact surface wave sensitivity kernels for windowed/tapered measurements at a specific frequency requires information of the scattered waveform kernel $\mathcal{K}^m(\mathbf{x}, \omega)$ and the spectra of the unperturbed ray $s(\omega)$ at nearby frequencies (eqs 4.7, 4.8 and 4.15). The width of the frequency band over which these quantities are needed depends upon the spectral properties of the window/taper. To avoid aliasing, one needs to sample the spectrum finely enough, and the computations introduced by this process can be time-consuming. In this section, we describe a useful and computationally efficient approximation, which requires the computation of $\mathcal{K}^m(\mathbf{x}, \omega)$ and $s(\omega)$ only at the frequency ω at which the measurements $\delta d(\omega)$ are made.

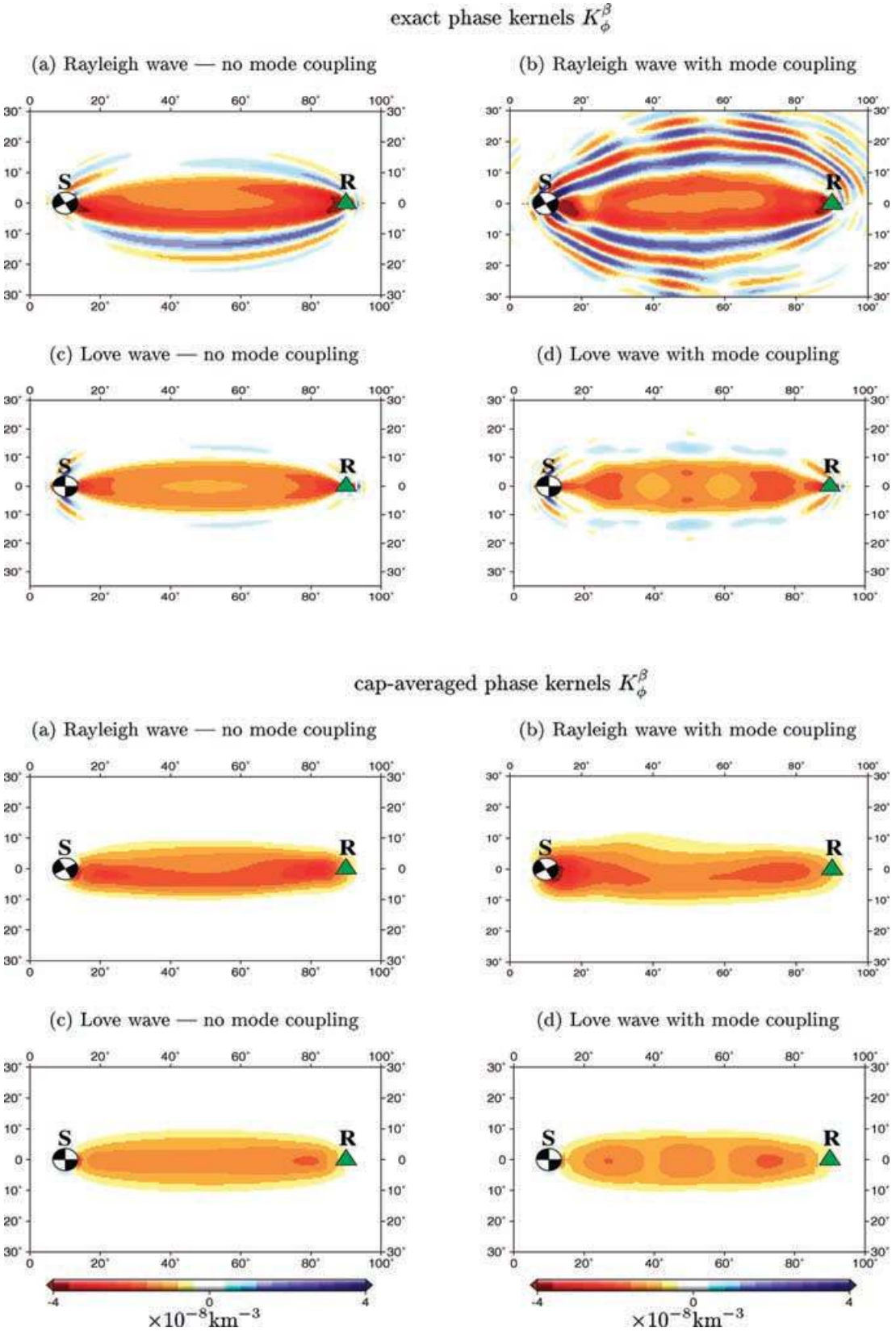

Figure 13. Mode-coupling effects on the phase-delay sensitivity kernels K_ϕ^β. The phase kernels of 6 mHz Rayleigh waves (a, b) and 6 mHz Love waves (c, d) are plotted at a depth of 192 km. The cap-averaged kernels (bottom) are the 'smoothed' version of the exact kernels (top), obtained by averaging the exact sensitivity kernel over a circular cap with a radius of 6°. The sensitivity kernels are for phase-delay measurements made using an 800 s cosine taper. In (a) and (b) the seismic source is a strike-slip fault at 52 km depth; the Rayleigh wave source radiation pattern is non-symmetric with respect to the reference ray; the angle between the maximum radiation direction and the geometrical ray is 15°. In (c) and (d), the seismic source is a strike-slip fault at 7 km depth; the Love wave radiation is symmetric, and maximum in the geometrical ray direction. The significance of mode-coupling effects is reduced in the cap-averaged kernels.

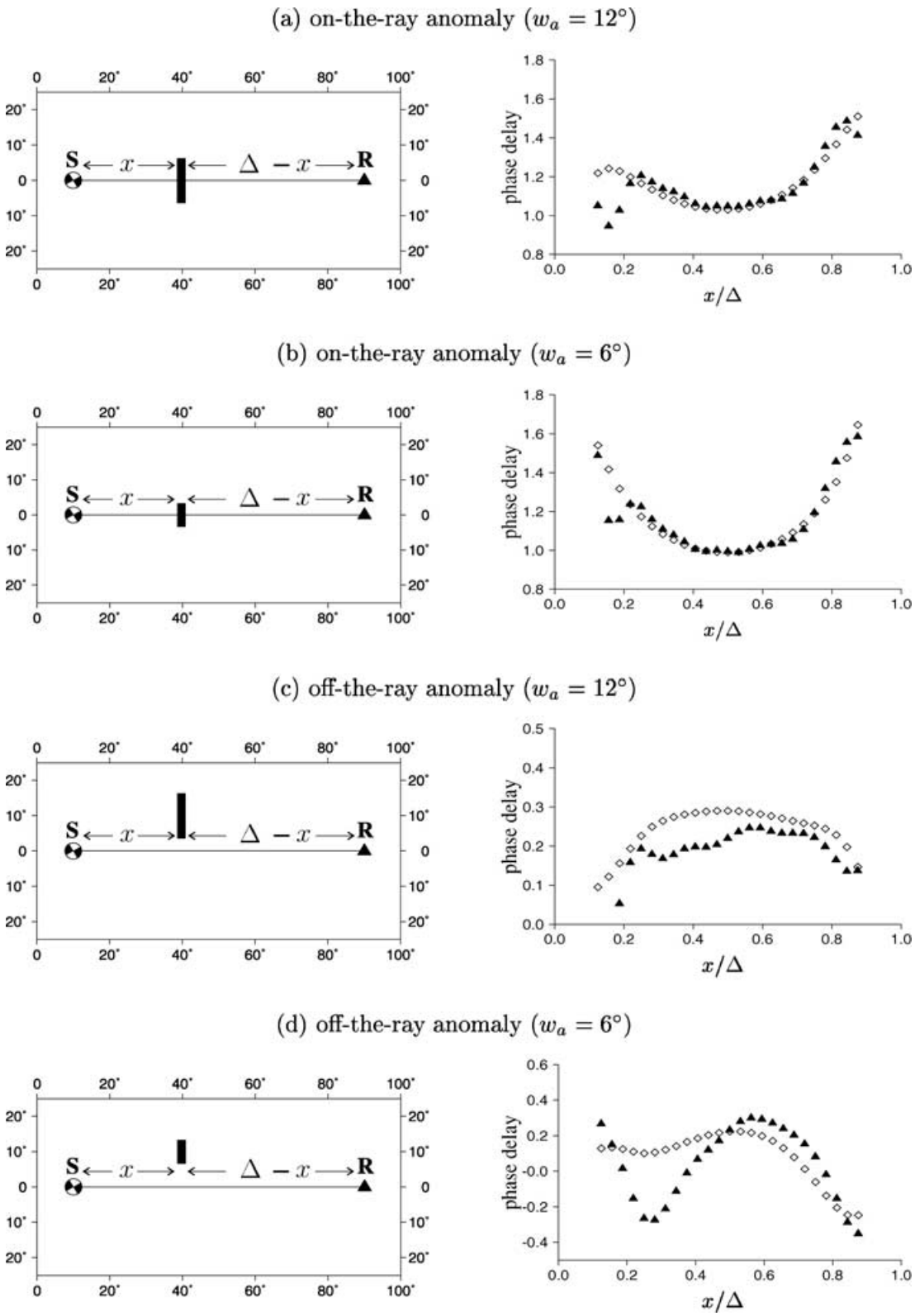

Figure 14. Mode-coupling effects on phase delays for anomalies on and off the geometrical ray. Left: Maps of anomaly locations; the anomalies extend in depth throughout the sensitivity region of the 6 mHz Rayleigh waves. Right: Phase delays computed with (triangle) and without (diamond) mode-coupling effects for 6 mHz Rayleigh waves. The sensitivity kernels K_ϕ^β are shown in Fig. 13(top). The velocity perturbation $\delta\beta/\beta$ of the anomaly is 2.5 per cent in (a) and (c), and 5 per cent in (b) and (d). The quantity $\Delta = 80^\circ$ is the source–receiver epicentral distance, and x is the source–scatterer distance projected onto the geometrical reference ray. The anomalies are 10° off the ray in (c) and (d). For the on-the-ray anomalies in (a) and (b), mode-coupling effects are significant in regions close to the source and receiver. For the off-the-ray anomalies in (c) and (d), mode-coupling effects do not exhibit a strong spatial dependence; the magnitude of the phase delays caused by the off-ray anomalies are much smaller than those caused by the on-the-ray anomalies.

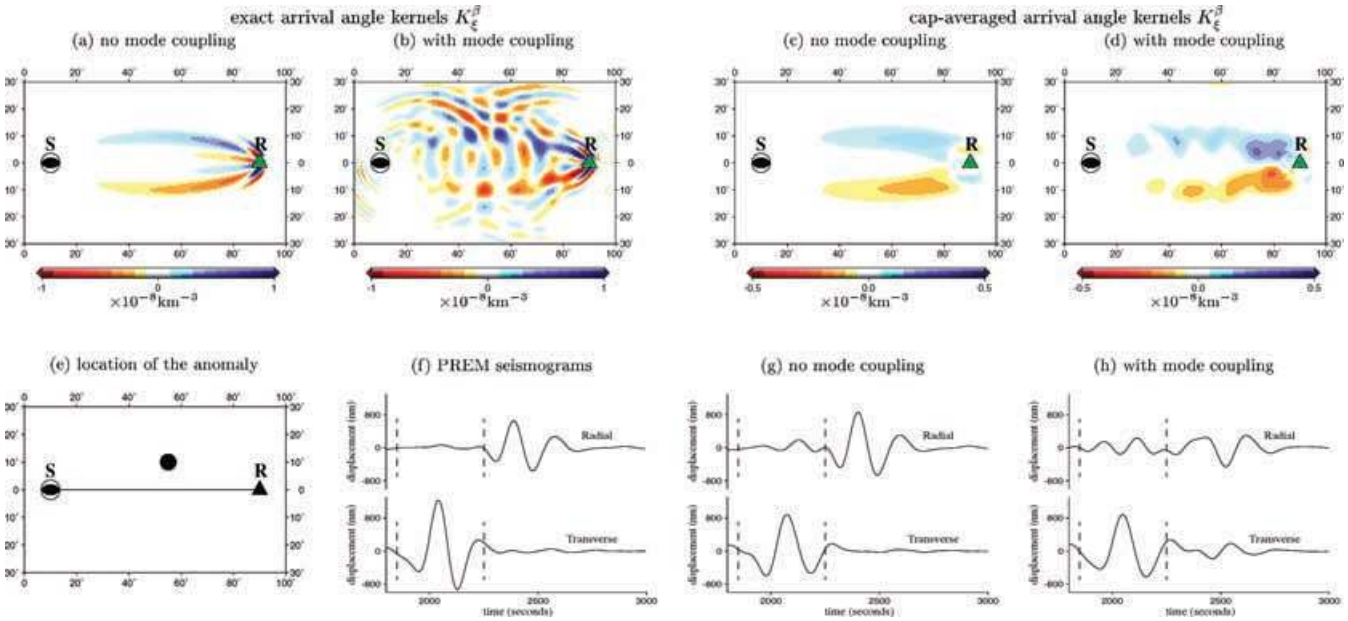

Figure 15. Mode-coupling effects on the arrival-angle sensitivity kernels K_ξ^β. (a), (b) The exact arrival-angle kernels for 6 mHz radial- and transverse-component Love wave measurements, made using a 400 s cosine taper; the taper position is indicated by the dashed lines superimposed on the PREM seismograms (f). The sensitivity kernels are plotted at a depth of 192 km. (c), (d) The result of cap-averaging the kernels in (a) and (b); the radius of the circular cap is 6°. The seismic source is a 45° dip-slip fault at 7 km depth (see beachball symbol). To illustrate the significance of mode coupling, seismograms (g) and (h) are computed for a slow anomaly with constant $\delta\beta/\beta = -50$ per cent. The anomaly (e) has a cylindrical shape, with a radius of 3°; it extends in depth throughout the sensitive region of the 6 mHz Love waves.

Using our Fourier sign convection, the jth taper in the time domain, $h_j(t)$, and its spectrum, $h_j(\omega)$, are related by

$$h_j(t) = \frac{1}{2\pi}\int_{-\infty}^{\infty} h_j(\omega)\mathrm{e}^{i\omega t}\,d\omega. \tag{9.1}$$

The tapered displacement spectrum of the unperturbed ray $s_j(\omega)$ is

$$s_j(\omega) = s(\omega)\otimes h_j(\omega) = \frac{1}{2\pi}\int_{-\infty}^{\infty} h_j(\nu)s(\omega-\nu)\,d\nu. \tag{9.2}$$

The untapered spectrum $s(\omega)$ is given in eq. (2.26), which we rewrite here using an amplitude-and-phase format:

$$s(\omega) = \mathcal{A}(\omega)\mathrm{e}^{-ik(\omega)\Delta}, \tag{9.3}$$

where $\mathcal{A}(\omega)$ represents all of the quantities on the right-hand side of eq. (2.26), except for the phase term $\mathrm{e}^{-ik(\omega)\Delta}$. We assume that the transformed tapers $h_j(\omega)$ are narrowly concentrated in the frequency domain, and make the following approximations:

$$\mathcal{A}(\omega-\nu) \approx \mathcal{A}(\omega), \tag{9.4}$$

$$k(\omega-\nu) \approx k(\omega) - \nu(\partial k/\partial\omega) = k(\omega) - \nu/C(\omega), \tag{9.5}$$

where $C(\omega) = d\omega/dk$ is the group velocity in rad s^{-1} measured on the unit sphere. Upon substituting eqs (9.3)–(9.5) into eq. (9.2), we obtain

$$\begin{aligned} s_j(\omega) &\approx \frac{1}{2\pi}\int_{-\infty}^{\infty} h_j(\nu)\mathcal{A}(\omega)\mathrm{e}^{-ik(\omega)\Delta}\mathrm{e}^{i\nu\Delta/C(\omega)}\,d\nu \\ &= \mathcal{A}(\omega)\mathrm{e}^{-ik(\omega)\Delta}\frac{1}{2\pi}\int_{-\infty}^{\infty} h_j(\nu)\mathrm{e}^{i\nu\Delta/C(\omega)}\,d\nu \\ &= s(\omega)h_j[t=\Delta/C(\omega)], \end{aligned} \tag{9.6}$$

where $h_j[t=\Delta/C(\omega)]$ is the jth time domain taper evaluated at the group arrival time $t=\Delta/C(\omega)$ for waves of frequency ω. Comparing eq. (9.6) with eq. (9.2), we see that this approximation amounts to replacement of the frequency-domain convolution operator '$\otimes h(\omega)$' by the multiplication operator '$\times h[t=\Delta/C(\omega)]$'. Employing the same approximation scheme for the scattered waveform kernel $\mathcal{K}^m(\mathbf{x},\omega)$, we obtain

$$\mathcal{K}^m(\mathbf{x},\omega)\otimes h_j(\omega) = \mathcal{K}^m(\mathbf{x},\omega)h_j[t=\Delta'/C'(\omega)+\Delta''/C''(\omega)], \tag{9.7}$$

where $\Delta'/C'(\omega)$ and $\Delta''/C''(\omega)$ are the group traveltimes of the scattered waves along the source-to-scatterer and the scatterer-to-receiver paths; $C'(\omega)$ and $C''(\omega)$ are the group velocities of surface wave modes σ' and σ'', evaluated at the measurement frequency ω; and the quantity $h_j[t=\Delta'/C'(\omega)+\Delta''/C''(\omega)]$ is the jth time-domain taper evaluated at the group arrival time of the scattered wave. By making the approximation

(9.4)–(9.5), the frequency domain convolution in calculating the sensitivity kernels for tapered measurements is reduced to a simple time-domain multiplication, which requires the computation of $\mathcal{K}^m(\mathbf{x}, \omega)$ and $s(\omega)$ only at the frequency ω at which the measurements are made.

In Fig. 16, we compare the approximate and the exact sensitivity kernels $K_\phi^\beta(\mathbf{x}, \omega)$ for 10 mHz and 4 mHz Love wave measurements, made using 800 s cosine tapers centred upon the group arrival times. In general, the two sensitivity kernels are in good agreement. There is a slight discrepancy in the 4 mHz phase kernels, due to the strong dispersion of these low-frequency waves. It also should be borne in mind that the accuracy of this approximation depends upon the length of the taper. Sensitivity kernels for measurements made using a shorter window require convolution over a wider frequency range, and the approximation in eqs (9.4) and (9.5) may not be adequate. However, in the practice of global surface wave tomography, the windows used in making phase and amplitude measurements generally have narrowly concentrated spectra (Laske & Masters 1996), and we expect the approximation to be adequate for those measurements. Surface wave arrival-angle perturbations are typically measured with a much shorter window, and accurate computation of their sensitivity kernels may require more time-consuming convolution in the frequency domain.

10 DISCUSSION AND CONCLUSION

We have shown how to compute 3-D sensitivity kernels for fundamental-mode surface wave phase, amplitude and arrival-angle measurements, based upon a propagating-wave version of the Born approximation in an isotropic, elastic reference earth model. We have derived the sensitivity kernels for multitaper measurements, though the results also apply to single-frequency measurements as a special case. The 3-D geometry of the sensitivity kernels depends upon the source–receiver distance, the measured wave train and frequency, and the source radiation pattern, as well as the tapering processes applied in making the measurements.

A forward-scattering approximation has been used to reduce the exact 3-D sensitivity kernels $K_d^{\alpha,\beta,\rho}(\mathbf{x}, \omega)$ to 2-D kernels $K_d^c(\hat{\mathbf{r}}, \omega)$, expressing the sensitivity to local phase-velocity perturbations. If the anomaly field varies weakly over space, so that the size of a characteristic anomaly is much larger than the width of the first Fresnel zone, the 2-D sensitivity kernels can be further reduced analytically to 1-D ray-theoretical kernels. Numerical experiments verify that when the size of the anomaly is much larger than the width of the first the Fresnel zone the 3-D Born sensitivities converge to ray theory. The convergence to ray theory for amplitude and arrival-angle measurements is slower than for phase-delay measurements.

Numerical experiments show that mode-coupling effects on phase measurements are most significant in regions close to the source and the receiver. Although a complete sensitivity computation requires mode-coupling effects to be included, the computational expense increases as N^2, where N is the number of surface wave modes at the measurement frequency. This is computationally expensive, especially for relatively high-frequency (e.g., >10 mHz) measurements, where more than 25 surface wave modes may need to be included. In practice, the importance of mode coupling depends upon the desired resolution of the structural heterogeneities. At the current stage of global surface wave tomography it is probably safe to neglect the effects of mode coupling on phase measurements for two reasons: (1) as a result of limited data availability, the desired resolution of the earth model does not require the fine structure of the sensitivity; the use of 3-D parametrization coarser than the sensitivity scale acts to smear out the effects of mode coupling; and (2) the number of measurements affected by mode coupling is likely to be relatively small in hand-picked data sets. Mode-coupling effects may, on the other hand, be significant in tomographic inversions incorporating arrival-angle measurements, even when the resolution is limited to large-scale structure. To speed up the computation of the sensitivity kernels for a large global surface wave data set we have developed a fast computational scheme, which transforms the frequency-domain convolution into a simple time-domain multiplication provided that the tapers used in making the measurements have a relatively narrow spectral concentration. There is no longer any reason to rely upon geometrical ray theory in surface wave tomographic inversions.

ACKNOWLEDGMENTS

YZ wishes to thank Shu-Huei Hung and Gabi Laske for helpful discussions. The reviewers, Wolfgang Friederich and Kazu Yoshizawa, and the Associate Editor, Rob van der Hilst, provided a number of thoughtful and constructive suggestions, which significantly improved the manuscript. This research was financially supported by the US National Science Foundation under grant EAR-0105387. All maps were generated using the Generic Mapping Tools (GMT) (Wessel & Smith 1995).

REFERENCES

Clévédé, É., Mégnin, C., Romanowicz, B. & Lognonné, P., 2000. Seismic waveform modeling and surface wave tomography in a three-dimensional Earth: asymptotic and non-asymptotic approaches, *Phys. Earth planet. Inter.,* **119,** 37–56.

Capdeville, Y., Stutzmann, E. & Montagner, J.P., 2000. Effect of a plume on long period surface waves computed with normal modes coupling, *Phys. Earth planet. Inter.,* **119,** 57–74.

Dahlen, F.A., 1987. Multiplet coupling and the calculation of synthetic long-period seismograms, *Geophys. J. R. astr. Soc.,* **91,** 241–254.

Dahlen, F.A. & Baig, A.M., 2002. Fréchet kernels for body wave amplitudes, *Geophys. J. Int.,* **150,** 440–466.

Dahlen, F.A. & Tromp, J., 1998. *Theoretical Global Seismology,* Princeton University Press, Princeton, NJ.

Dahlen, F.A., Hung, S.-H. & Nolet, G., 2000. Fréchet kernels for finite-frequency travel times—I. Theory, *Geophys. J. Int.,* **141,** 157–174.

Dalkolmo, J. & Friederich, W., 2000. Born scattering of long-period body waves, *Geophys. J. Int.,* **142,** 876–888.

Ekström, G., Tromp, J. & Larson, E.W.F., 1997. Measurements and global models of surface wave propagation, *J. geophys. Res.,* **102,** 8137–8157.

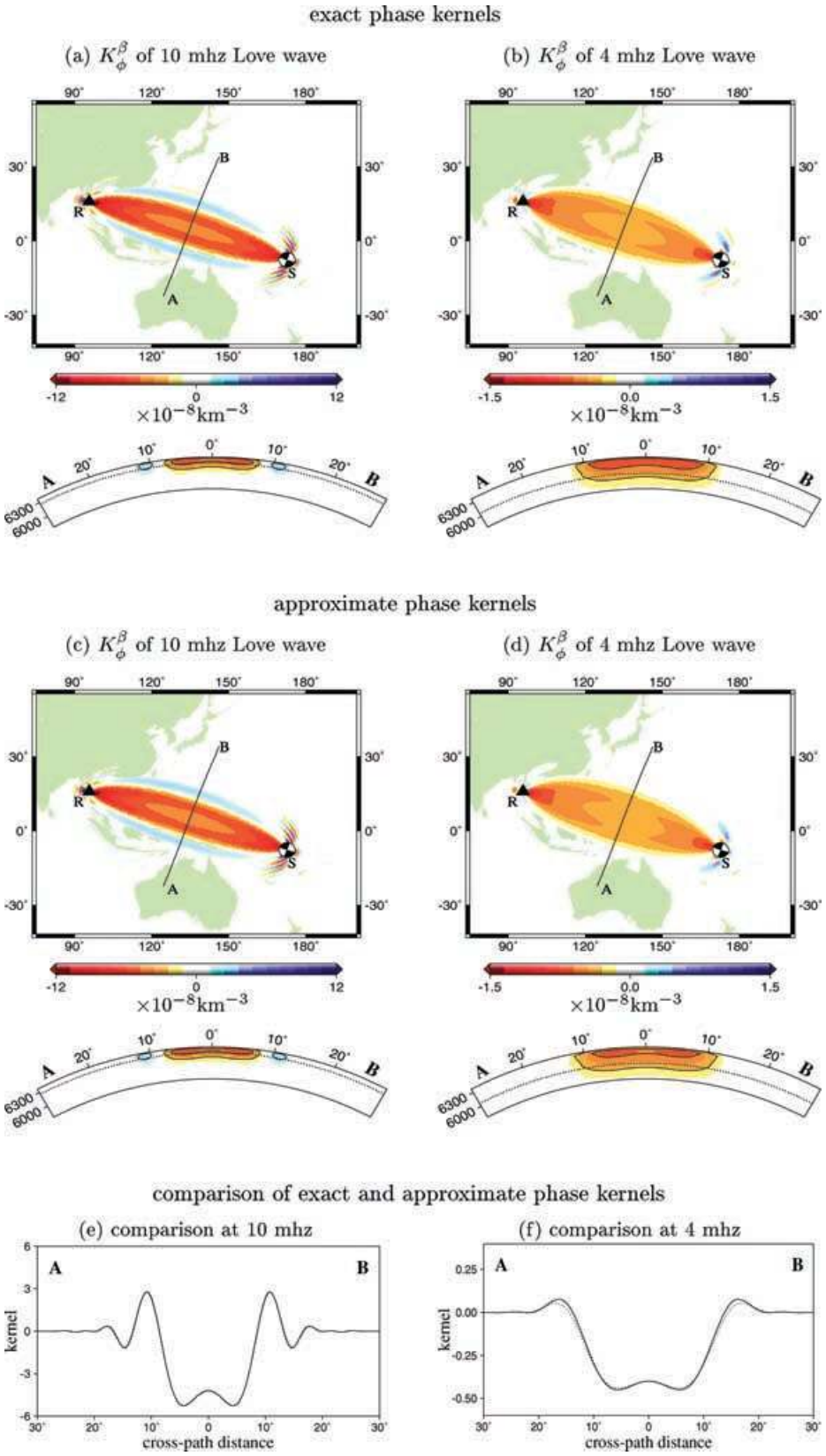

Figure 16. (a), (b) Map views of the exact phase kernels for 10 mHz and 4 mHz Love waves, excited by a strike-slip source at a depth of 52 km; the sensitivity kernels are plotted at 108 km and 310 km respectively; the slice views are AB cross-sections, with the dashed lines plotted at the depths of the map views. (c), (d) The sensitivity kernels computed using the fast computational approach described in Section 9. (e), (f) The excellent agreement between the exact kernels and the approximate kernels in the AB cross-sections at depths of 108 km and 310 km. The kernels are for Love wave measurements made using 800 s cosine tapers, centred on the group arrival time predicted by PREM.

Friederich, W., 1999. Propagation of seismic shear and surface waves in a laterally heterogeneous mantle by multiple forward scattering, *Geophys. J. Int.,* **136,** 180–204.

Friederich, W., Wielandt, E. & Stange, S., 1993. Multiple forward scattering of surface waves: comparison with an exact solution and Born single-scattering methods, *Geophys. J. Int.,* **112,** 264–275.

Hung, S.-H., Dahlen, F.A. & Nolet, G., 2000. Fréchet kernels for finite-frequency travel times—II. Examples, *Geophys. J. Int.,* **141,** 175–203.

Kárason, H. & van der Hilst, R. D., 2001. Tomographic imaging of the lowermost mantle with differential times of refracted and diffracted core phases (*PKP*, $P_{\rm diff}$), *J. geophys. Res.,* **106,** 6569–6587.

Larson, E.W.F. & Ekström., G., 2002. Determining surface wave arrival angle anomalies, *J. geophys. Res.,* **107**(B6), doi:10.1029/2000JB000048.

Laske, G., 1995. Global observation of off-great-circle propagation of long-period surface waves, *Geophys. J. Int.,* **123,** 245–259.

Laske, G. & Masters, G., 1996. Constraints on global phase velocity maps from long-period polarization data, *J. geophys. Res.,* **101,** 16 059–16 075.

Laske, G., Masters, G. & Zürn, W., 1994. Frequency-dependent polarization measurements of long-period surface waves and their implications for global phase velocity maps, *Phys. Earth planet. Inter.,* **84,** 111–137.

Marquering, H., Dahlen, F.A. & Nolet. G., 1999. Three-dimensional sensitivity kernels for finite-frequency traveltimes: the banana–doughnut paradox, *Geophys. J. Int.,* **137,** 805–815.

Marquering, H., Nolet, G. & Dahlen, F.A., 1998. Three-dimensional waveform sensitivity kernels, *Geophys. J. Int.,* **132,** 521–534.

Meier, T., Lebedev, S., Nolet, G. & Dahlen, F.A., 1997. Diffraction tomography using multimode surface waves, *J. geophys. Res.,* **102,** 8255–8267.

Montelli, R., Nolet, G., Masters, G., Dahlen, F.A., & Hung, S.-H., 2003. Global *P* and *PP* traveltime tomography: rays versus waves, *Geophys. J. Int.,* in press.

Park, J., Vernon, F.L. III & Lindberg, C.R., 1987. Frequency dependent polarization analysis of high-frequency seismograms, *J. geophys. Res.,* **92,** 12 664–12 674.

Ritzwoller, M.H., Shapiro, N.M., Barmin, M.P. & Levshin, A.L., 2002. Global surface wave diffraction tomography, *J. geophys. Res.,* **107**(B12), doi:10.1029/2002JB001777.

Romanowicz, B., 1987. Multiplet-multiplet coupling due to lateral heterogeneity: asymptotic effects on the amplitude and frequency of the Earth's normal modes, *Geophys. J. R. astr. Soc.,* **90,** 75–100.

Slepian, D., 1978. Prolate spheroidal wave functions, Fourier analysis, and uncertainty. V: The discrete case, *Bell Syst. Tech. J.,* **57,** 1371–1430.

Snieder, R., 1986. 3-D linearized scattering of surface waves and a formalism for surface wave holography, *Geophys. J. R. astr. Soc.,* **84,** 581–605.

Snieder, R. & Nolet, G., 1987. Linearized scattering of surface waves on a spherical Earth, *J. geophys.,* **61,** 55–63.

Spetzler, J., Trampert, J. & Snieder, R., 2001. Are we exceeding the limits of the great circle approximation in global surface wave tomography?, *Geophys. Res. Lett.,* **28,** 2341–2344.

Spetzler, J., Trampert, J. & Snieder, R., 2002. The effects of scattering in surface wave tomography, *Geophys. J. Int.,* **149,** 755–767.

Thomson, D.J., 1982. Spectrum estimation and harmonic analysis, *IEEE Proc.,* **70,** 1055–1096.

Tromp, J. & Dahlen, F.A., 1992. Variational principles for surface wave propagation on a laterally heterogeneous Earth—II. Frequency-domain JWKB theory, *Geophys. J. Int.,* **109,** 599–619.

Wang, Z. & Dahlen, F.A., 1995. Validity of surface wave ray theory on a laterally heterogeneous Earth, *Geophys. J. Int.,* **123,** 757–773.

Wessel, P. & Smith, W.H.F., 1995. New version of the Generic Mapping Tools released, *EOS, Trans. Am. geophys. Un.,* **76,** 329.

Woodhouse, J.H. & Girnius, T.P., 1982. Surface waves and free-oscillations in a regionalized earth mode, *Geophys. J. R. astr. Soc.,* **68,** 653–673.

Woodhouse, J.H. & Wong, Y.K., 1986. Amplitudes, phase and path anomalies of mantle waves, *Geophys. J. R. astr. Soc.,* **87,** 753–773.

Yomogida, K., 1992. Fresnel zone inversion for lateral heterogeneities in the Earth, *Pure appl. Geophys.,* **138,** 391–406.

Yomogida, K. & Aki, K., 1987. Amplitude and phase data inversions for phase velocity anomalies in the Pacific Ocean basin, *Geophys. J. R. astr. Soc.,* **88,** 161–204.

Yoshizawa, K. & Kennett, B.L.N., 2002. Determination of the influence zone for surface wave paths, *Geophys. J. Int.,* **149,** 440–453.

Yoshizawa, K., Yomogida, K., & Tsuboi, S., 1999. Resolving power of surface wave polarization data for higher-order heterogeneities, *Geophys. J. Int.,* **138,** 205–220.

Zhao, L., Jordan, T.H. & Chapman, C.H., 2000. Three-dimensional Fréchet differential kernels for seismic delay times, *Geophys. J. Int.,* **141,** 558–576.

APPENDIX A: THE SCATTERING COEFFICIENT

The interaction coefficient based on the Born approximation, given in eq. (2.16), is rewritten below:

$$ {}_{\sigma'}\Omega_{\sigma''} = \delta\rho\omega^2 \mathbf{p}'\cdot\mathbf{p}''^{*} - \delta\lambda(\mathrm{tr}\,\boldsymbol{E}')\,(\mathrm{tr}\,\boldsymbol{E}''^{*}) - 2\delta\mu(\boldsymbol{E}'\colon \boldsymbol{E}''^{*}), \tag{A1}$$

where the asterisk denotes the complex conjugate; and where $\mathbf{p}' = \hat{\mathbf{r}}U' - i\hat{\mathbf{k}}'V' + i(\hat{\mathbf{r}}\times\hat{\mathbf{k}}')W'$ is the polarization vector of surface wave mode σ' along the source-to-scatterer leg; and $\mathbf{p}'' = \hat{\mathbf{r}}U'' - i\hat{\mathbf{k}}''V'' + i(\hat{\mathbf{r}}\times\hat{\mathbf{k}}'')W''$ is the polarization vector of surface wave mode σ'' along the scatterer-to-receiver leg. The quantity $\boldsymbol{E} = (1/2)[\nabla\mathbf{p} + (\nabla\mathbf{p})^{\mathrm{T}}]$ is the surface wave strain tensor. All quantities in eq. (A1) are evaluated at the scatterer. Using the relations in eq. (2.3), rewritten here for convenience,

$$2\rho\alpha\delta\alpha = \delta\lambda + 2\delta\mu - \alpha^2\delta\rho, \quad 2\rho\beta\delta\beta = \delta\mu - \beta^2\delta\rho, \tag{A2}$$

the scattering coefficient ${}_{\sigma'}\Omega_{\sigma''}$ can be transformed into a linear combination of the fractional model perturbations of $\delta\alpha/\alpha$, $\delta\beta/\beta$ and $\delta\rho/\rho$:

$$ {}_{\sigma'}\Omega_{\sigma''} = -2\rho\alpha^2(\mathrm{tr}\,\boldsymbol{E}')\,(\mathrm{tr}\,\boldsymbol{E}''^{*})\left(\frac{\delta\alpha}{\alpha}\right) + \left[4\rho\beta^2(\mathrm{tr}\,\boldsymbol{E}')(\mathrm{tr}\,\boldsymbol{E}''^{*}) - 4\rho\beta^2(\boldsymbol{E}'\colon \boldsymbol{E}''^{*})\right]\left(\frac{\delta\beta}{\beta}\right)$$

$$+\left[\rho(2\beta^2-\alpha^2)(\mathrm{tr}\,\boldsymbol{E}')(\mathrm{tr}\,\boldsymbol{E}''^{*}) - 2\rho\beta^2(\boldsymbol{E}'\colon \boldsymbol{E}''^{*}) + \rho\omega^2\mathbf{p}'\cdot\mathbf{p}''^{*}\right]\left(\frac{\delta\rho}{\rho}\right). \tag{A3}$$

In brief,

$$ {}_{\sigma'}\Omega_{\sigma''} = {}_{\sigma'}\Omega^{\alpha}_{\sigma''}\left(\frac{\delta\alpha}{\alpha}\right) + {}_{\sigma'}\Omega^{\beta}_{\sigma''}\left(\frac{\delta\beta}{\beta}\right) + {}_{\sigma'}\Omega^{\rho}_{\sigma''}\left(\frac{\delta\rho}{\rho}\right). \tag{A4}$$

The detailed expressions of the scattering coefficients ${}_{\sigma'}\Omega^{\alpha}_{\sigma''}$, ${}_{\sigma'}\Omega^{\beta}_{\sigma''}$ and ${}_{\sigma'}\Omega^{\rho}_{\sigma''}$ are:

For Love-to-Love scattering,

$$ {}_{\sigma'}\Omega^{\alpha}_{\sigma''} = 0; \tag{A5}$$

$$
\begin{aligned}
{}_{\sigma'}\Omega^{\beta}_{\sigma''} &= -2\rho\beta^2(\dot{W}' - r^{-1}W')(\dot{W}'' - r^{-1}W'')\cos\eta \\
&\quad - 2\rho\beta^2 k' k'' r^{-2} W' W'' \cos 2\eta;
\end{aligned} \tag{A6}
$$

$$
\begin{aligned}
{}_{\sigma'}\Omega^{\rho}_{\sigma''} &= \rho\omega^2 W' W'' \cos\eta \\
&\quad - \rho\beta^2(\dot{W}' - r^{-1}W')(\dot{W}'' - r^{-1}W'')\cos\eta \\
&\quad - \rho\beta^2 k' k'' r^{-2} W' W'' \cos 2\eta;
\end{aligned} \tag{A7}
$$

for Rayleigh-to-Rayleigh scattering,

$$
{}_{\sigma'}\Omega^{\alpha}_{\sigma''} = -2\rho\alpha^2(\dot{U}' + 2r^{-1}U' - k' r^{-1} V')\,(\dot{U}'' + 2r^{-1}U'' - k'' r^{-1} V''); \tag{A8}
$$

$$
\begin{aligned}
{}_{\sigma'}\Omega^{\beta}_{\sigma''} &= 4\rho\beta^2(\dot{U}' + 2r^{-1}U' - k' r^{-1} V')\,(\dot{U}'' + 2r^{-1}U'' - k'' r^{-1} V'') \\
&\quad - 2\rho\beta^2[2\dot{U}'\dot{U}'' + r^{-2}(2U' - k' V')(2U'' - k'' V'')] \\
&\quad - 2\rho\beta^2(\dot{V}' - r^{-1}V' + k' r^{-1} U')\,(\dot{V}'' - r^{-1}V'' + k'' r^{-1} U'')\cos\eta \\
&\quad - 2\rho\beta^2 k' k'' r^{-2} V' V'' \cos 2\eta;
\end{aligned} \tag{A9}
$$

$$
\begin{aligned}
{}_{\sigma'}\Omega^{\rho}_{\sigma''} &= \rho\omega^2(U' U'' + V' V'' \cos\eta) \\
&\quad - \rho\beta^2[2\dot{U}'\dot{U}'' + r^{-2}(2U' - k' V')(2U'' - k'' V'')] \\
&\quad - \rho(\alpha^2 - 2\beta^2)(\dot{U}' + 2r^{-1}U' - k' r^{-1} V')(\dot{U}'' + 2r^{-1}U'' - k'' r^{-1} V'') \\
&\quad - \rho\beta^2(\dot{V}' - r^{-1}V' + k' r^{-1} U')(\dot{V}'' - r^{-1}V'' + k'' r^{-1} U'')\cos\eta \\
&\quad - \rho\beta^2 k' k'' r^{-2} V' V'' \cos 2\eta;
\end{aligned} \tag{A10}
$$

for Love-to-Rayleigh scattering,

$$
{}_{\sigma'}\Omega^{\alpha}_{\sigma''} = 0; \tag{A11}
$$

$$
\begin{aligned}
{}_{\sigma'}\Omega^{\beta}_{\sigma''} &= 2\rho\beta^2(\dot{W}' - r^{-1}W')(\dot{V}'' - r^{-1}V'' + k'' r^{-1} U'')\sin\eta \\
&\quad + 2\rho\beta^2 k' k'' r^{-2} W' V'' \sin 2\eta;
\end{aligned} \tag{A12}
$$

$$
\begin{aligned}
{}_{\sigma'}\Omega^{\rho}_{\sigma''} &= -\rho\omega^2 W' V'' \sin\eta \\
&\quad + \rho\beta^2(\dot{W}' - r^{-1}W')(\dot{V}'' - r^{-1}V'' + k'' r^{-1} U'')\sin\eta \\
&\quad + \rho\beta^2 k' k'' r^{-2} W' V'' \sin 2\eta;
\end{aligned} \tag{A13}
$$

for Rayleigh-to-Love scattering,

$$
{}_{\sigma'}\Omega^{\alpha}_{\sigma''} = 0; \tag{A14}
$$

$$
\begin{aligned}
{}_{\sigma'}\Omega^{\beta}_{\sigma''} &= -2\rho\beta^2(\dot{V}' - r^{-1}V' + k' r^{-1} U')(\dot{W}'' - r^{-1}W'')\sin\eta \\
&\quad - 2\rho\beta^2 k' k'' r^{-2} V' W'' \sin 2\eta;
\end{aligned} \tag{A15}
$$

$$
\begin{aligned}
{}_{\sigma'}\Omega^{\rho}_{\sigma''} &= \rho\omega^2 V' W'' \sin\eta \\
&\quad - \rho\beta^2(\dot{V}' - r^{-1}V' + k' r^{-1} U')(\dot{W}'' - r^{-1}W'')\sin\eta \\
&\quad - \rho\beta^2 k' k'' r^{-2} V' W'' \sin 2\eta.
\end{aligned} \tag{A16}
$$

The quantity $\eta = \arccos(\hat{\mathbf{k}}' \cdot \hat{\mathbf{k}}'')$ is the scattering angle, measured counter-clockwise from $\hat{\mathbf{k}}'$ to $\hat{\mathbf{k}}''$ (Fig. 1).